

**Shell effects in high-energy atomic scattering**M. V. Bondarenco <sup>\*</sup>*NSC Kharkov Institute of Physics and Technology, 1 Academic Street, 61108 Kharkov, Ukraine  
and V. N. Karazin Kharkov National University, 4 Svobody Square, 61077 Kharkov, Ukraine*

(Received 26 May 2023; accepted 22 August 2023; published 12 September 2023)

Shell effects in the differential cross section of fast charged particle scattering on an atom are studied as deviations of the Hartree-Fock mean atomic potential predictions from those for the Thomas-Fermi atom. Significant deviations of that kind are found at moderate momentum transfers, where they are caused by intermediate atomic shells and regularly oscillate with  $Z$ , and also for hard-scattering observables, where they are caused by inner shells (relativistic at high  $Z$ ) and depend on  $Z$  monotonically. In application to multiple Coulomb scattering in thick targets, shell corrections to the Molière screening angle are calculated. They are found to pick up commensurable contributions from inner and outer shells, leading to superposed monotonic and oscillatory deviations from the Thomas-Fermi prediction.

DOI: [10.1103/PhysRevA.108.032813](https://doi.org/10.1103/PhysRevA.108.032813)**I. INTRODUCTION**

Scattering of fast particles on atoms of most chemical elements, owing to their large atomic numbers ( $Z \gg 1$ ), is predominantly elastic and ruled by the mean atomic potential. The highest sensitivity of the atomic scattering differential cross section to the shape of the potential is achieved in the Born approximation, when only one virtual photon is exchanged between the projectile particle and a single atom in the target. The scattering differential cross section is then proportional to the modulus square of the atomic form factor, equal to the Fourier transform of the spatial density of atomic electrons [1,2]. This relationship is used for direct experimental determination of atomic electron distributions, which can be compared with accurate theoretical predictions based on Hartree-Fock calculations [3,4], etc.

In practical targets, however, projectile particles are often beyond the single-scattering regime. That may be due to the large target thickness or/and moderate particle velocity. If the traversed target is thicker than a few nanometers, successive interactions with different atoms happen, rendering the scattering plural or multiple. The random walk in momentum transfers washes out fine detail of the single-scattering contributions. Furthermore, if the Coulomb parameter  $Z_1 Z e^2 / \hbar v$  for single scattering of a particle with charge  $Z_1 e$  and velocity  $v$  is sizable, several photons will be exchanged with every atom. In any case, as the scattering becomes less perturbative, especially if it enters a classical regime, the sensitivity to the fine detail of the atomic potential is generally expected to diminish due to the integration along the trajectory of the penetrating particle. Assuming that, it has been common to describe particle passage through matter based on the Thomas-Fermi (TF) approximation for the atomic charge distribution, entirely neglecting the existence of atomic shells. A closer exami-

nation, however, reveals important scattering observables in which shell effects should persist. A few examples can be given.

A prominent feature of any atomic single-scattering differential cross section is its Rutherford power-law asymptotics at large momentum transfers. At high-energy small-angle multiple scattering in thick targets, it gives a logarithmically dominant contribution to the particle distribution also in the central region of angles. All the atomic screening effects are encapsulated there only to a constant next to the large logarithm, known as the Molière screening angle. There were early indications that the screening angle or the distribution width can deviate from its value in the TF approximation [5,6], but there do not yet seem to be definitive studies confirming these signs.

Finer details of the scattering differential cross section transpire if the target is made thinner. The scattering then keeps close to single in a wider range of momentum transfers  $q$ , which may include the region where the scattering appreciably deviates from Rutherford's. There atomic screening manifests itself as a power correction to the Rutherford asymptotics (the so-called weak-screening regime [7–9]). Since large  $q$  generally correspond to small distances from the atomic nucleus, weak screening must be determined predominantly by inner shells. Investigations of shell contributions to the weak-screening correction, however, do not seem to be forthcoming in the literature.

Deviations from the TF approximation may also arise in the low- $q$  region, around the maximum of the differential cross section. Low- $q$  shell corrections are expected to stem from intermediate or outer shells. However, even though such shells contain many electrons, their TF treatment may be too crude. An obvious example is the  $Z$  periodicity in the Periodic Table of Elements; yet the latter in its conventional form is related only to filling in of the outermost shell, whereas the existence of similar periodic behavior for intermediate shells is not so obvious. The theory of internal shell structure of many-electron atoms continues to develop [10–14].

<sup>\*</sup>m.bondarenco@desy.de

Sufficiently accurate conclusions about the magnitude of shell effects may be based on Hartree-Fock (HF) atom calculations. On applying HF densities to the description of hard scattering, one should generally be aware that at very small distances  $r$  from the nucleus the accuracy of the HF method can decrease. By now, though, substantial progress has been made in amending the emerging issues and improving the parametrization quality.

The aim of the present work is to investigate the nonperturbative scattering observables sensitive to shell effects, with the use of modern HF distributions, properly accounting for the electron density behavior close to the nucleus as well as relativistic effects. The structure of the paper is the following. In Sec. II A, after showing a comparison of TF and HF mean electron densities and illustrating the shape and the magnitude of shell effects, we set forth a description of fast classical particle scattering in the potential created by such charge distributions. In Sec. II B it is extended to quantum scattering. Thereupon, we turn to studying shell effects in scattering by selecting a few numbers best characterizing the gross behavior of the differential scattering cross section and scrutinizing their  $Z$  dependences. In Sec. III the region of intermediate momentum transfers is treated. There the differential cross section is found to significantly oscillate as a function of the atomic number  $Z$ . In Sec. IV the opposite case of large  $q$  is considered. The power correction to the Rutherford asymptotics is evaluated and found to be proportional to the atomic mean-inverse-square radius  $\langle r^{-2} \rangle$ , for which a formula is derived, capturing its monotonic  $Z$  dependence due to the accumulation of electrons in higher shells, along with an accelerated rise at high  $Z$  due to the relativism of inner shells. Section V scrutinizes shell corrections to Molière's screening angle, which is defined by an integral spanning a wide range of  $q$ . It is established that inner and intermediate shells contribute there together, leading to a low- $Z$  rise superposed on high- $Z$  oscillations. A summary is given in Sec. VI.

## II. HARTREE-FOCK VS THOMAS-FERMI DENSITIES: GENERAL DESCRIPTION OF HIGH-ENERGY SCATTERING

In this preliminary section we will render the description of high-energy atomic scattering a form most closely connected to the atomic electron distribution function, providing both classical and quantum-mechanical descriptions. At the same time, we will take the opportunity to visualize the differences between the HF and TF distributions themselves.

### A. Atomic potential screening function and charge-density distribution

The mean electrostatic field of an atom with the atomic number  $Z$  is described by a screened Coulomb potential

$$\varphi(r) = \frac{Ze}{r} g(Z, r), \quad (1)$$

where  $e > 0$  is the proton charge. The screening function  $g$  is everywhere positive, equals unity at the nucleus,

$$g(Z, 0) = 1, \quad (2)$$

and decreases with distance  $r$  from it. The mean potential  $\varphi$  is linearly induced by the mean electric charge density  $e[Z\delta(\mathbf{r}) - n_e(r)]$  in the atom, with  $n_e(r)$  the electron density. It thus obeys a Laplace equation

$$\Delta\varphi = 4\pi e[n_e(r) - Z\delta(\mathbf{r})]. \quad (3)$$

Having in mind applications to particle passage through ordinary matter, it is natural to assume the atom neutrality

$$\int d^3r n_e(r) = Z. \quad (4)$$

For a spherically symmetrical mean electron density  $n_e(r)$ , only the radial component of the Laplacian in (3) differs from zero:  $\Delta\varphi = \Delta_r\varphi = r^{-1} \frac{\partial^2}{\partial r^2}(r\varphi)$ . Equation (3) therefore is essentially an ordinary second-order differential equation for  $g$ :

$$g''(r) = \frac{4\pi}{Z} r n_e(r), \quad r > 0. \quad (5)$$

The boundary condition for a neutral atom is

$$g(Z, \infty) = 0. \quad (6)$$

Then (2) (which must actually hold as well for ions) is automatically retrieved from (6) and (4):

$$g(0) = \frac{4\pi}{Z} \int_0^\infty dr' \int_{r'}^\infty dr r n_e(r) = \frac{4\pi}{Z} \int_0^\infty dr r^2 n_e(r) = 1.$$

The distribution  $n_e(r)$  in turn depends on the potential  $\varphi(r)$ . Rigorously, they should be evaluated together beyond the mean-field level, in terms of multielectron wave functions. However, a few important corollaries from Eq. (5) can be drawn at once.

### 1. Constraints at $r = 0$

(a) While Eq. (5) is intrinsically classical,  $n_e(r)$  on its right-hand side is determined by quantum mechanics and consequently must be everywhere finite in the nonrelativistic case. It follows that the right-hand side of Eq. (5) must vanish in the origin due to the factor  $r$ ,

$$r n_e(r) \xrightarrow{r \rightarrow 0} 0, \quad (7)$$

and therefore

$$g''(0) = 0. \quad (8)$$

In a relativistic treatment and for a pointlike nucleus,  $n_e(r)$  blows up at  $r \rightarrow 0$ , but only weakly. It proves [15,16] that for any physical  $Z$  obeying

$$\sqrt{1 - (Ze^2/\hbar c)^2} > \frac{1}{2}, \quad (9)$$

the conditions (7) and (8) still remain valid.

(b) Another implication from the nonrelativistic quantum mechanics is Kato's theorem [17,18] (see Appendix A), relating the (logarithmic) derivative of the density of bound electrons at the nucleus to the nucleus charge

$$\frac{n'_e(0)}{n_e(0)} = -\frac{2Z}{a_B}, \quad (10)$$

where  $a_B = \hbar^2/m_e e^2 = 0.5292 \text{ \AA}$  stands for the Bohr radius. It holds for individual electron orbitals, being independent of

their energies, and is thus equally valid for the total electron density. Combined with Eq. (5), the relation (10) yields a constraint on the fourth derivative of the screening function

$$g^{(iv)}(0) = -\frac{4Z}{a_B} g'''(0) = -\frac{16\pi}{a_B} n_e(0). \quad (11)$$

## 2. Thomas-Fermi approximation

The simplest self-consistent-field approximation, customarily used as a reference one, is due to Thomas and Fermi [19]. It is purely local, in the sense that  $n_e(r)$  is determined by the electron potential energy  $-e\varphi(r)$  in the same spatial point  $r$ , i.e.,  $-e\varphi(r)$  is regarded as the depth of a physically broad potential well, which is completely (for a neutral atom) filled by the quasi-free-electron Fermi liquid. That supplies the equations

$$n_e(r) = 2 \frac{4\pi}{3} \left( \frac{p_{\max}(r)}{2\pi\hbar} \right)^3, \quad p_{\max}(r) = \sqrt{2me\varphi(r)}. \quad (12)$$

The system of equations (5) and (12) leads to a scaling of the  $r$  and  $Z$  dependences in terms of a single dimensionless variable

$$\xi(Z, r) = \frac{r}{a_{\text{TF}}(Z)}. \quad (13)$$

Here the Thomas-Fermi radius

$$a_{\text{TF}} = \frac{1}{2} \left( \frac{3\pi}{4} \right)^{2/3} Z^{-1/3} a_B = 0.885 Z^{-1/3} a_B \quad (14)$$

represents the characteristic  $Z$ -dependent spatial scale for this approximation. The universal (valid for all  $Z$ ) screening function

$$g(Z, r) = \phi_{\text{TF}}[\xi(Z, r)] \quad (15)$$

of the scaling radius  $\xi$  obeys the Thomas-Fermi equation [2,19]

$$\xi^{1/2} \phi_{\text{TF}}''(\xi) = \phi_{\text{TF}}^{3/2}(\xi) \quad (16)$$

subject to the boundary conditions following from (2) and (6):

$$\phi_{\text{TF}}(0) = 1, \quad \phi_{\text{TF}}(\infty) = 0. \quad (17)$$

The electron density is expressed in terms of  $\phi_{\text{TF}}$  as

$$n_e^{\text{TF}}(r) = \frac{Z}{4\pi a_{\text{TF}}^3} \left( \frac{\phi_{\text{TF}}(\xi)}{\xi} \right)^{3/2} \quad (18)$$

and automatically satisfies the normalization condition (4):

$$\begin{aligned} \int d^3r n_e^{\text{TF}}(r) &= Z \int_0^\infty d\xi \xi^{1/2} \phi_{\text{TF}}^{3/2} = Z \int_0^\infty d\xi \xi \phi_{\text{TF}}'' \\ &= Z \phi_{\text{TF}}(0) = Z. \end{aligned}$$

However compact and simple looking Eq. (16) may be, because of its nonlinearity, it needs to be solved numerically. Its computer solution, displayed in Fig. 1, will be used in what follows for comparison with HF calculations. For analysis of scattering with high momentum transfers, it is also necessary to know the small- $\xi$  asymptotics of  $\phi_{\text{TF}}$ , which is quoted in Eq. (B1). Its domain of applicability can be visualized from Fig. 1.

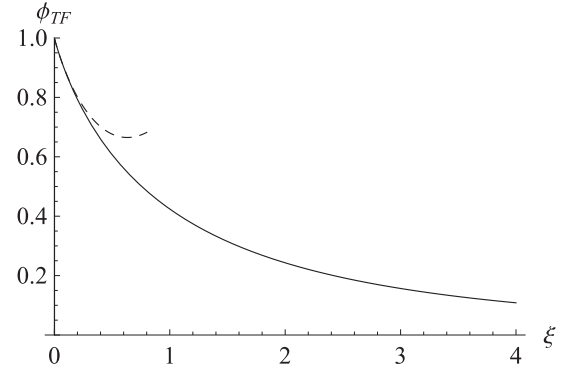


FIG. 1. Thomas-Fermi screening function vs its scaling variable  $\xi = r/a_{\text{TF}}(Z)$ . The solid curve shows the solution of Eq. (16) with boundary conditions (17) and the dashed the small- $\xi$  asymptotics (B1). The latter is observed to provide a satisfactory approximation for  $\xi < 0.3$ .

A known caveat is that the function  $\phi_{\text{TF}}$  obtained from Eqs. (16) and (17) behaves not quite physically at both large and small  $r$  (or  $\xi$ ) [2,19]. As is evident from Eqs. (18) and (17), the TF electron density blows up at the origin as  $n_e^{\text{TF}}(r) \sim r^{-3/2}$ , whereas rigorously in quantum mechanics [beyond the semiclassical approximation (12)] it must remain finite everywhere [cf. Eq. (10) and see Fig. 2(a)]. That might seem to be relatively harmless in application to  $g$ , as long as  $g(0) = \phi_{\text{TF}}(0) = 1$  and  $g'(0) = \phi_{\text{TF}}'(0)/a_{\text{TF}}$  are finite even in the TF approximation. However,  $\phi_{\text{TF}}'(0) = \infty$  strongly violates the condition (8). That in turn will affect the power index of the hard-scattering asymptotics, which we will be studying below, in Sec. IV.

## 3. Hartree-Fock electron density parametrizations

For our purposes, a sufficiently accurate description of electron densities can be obtained from relativistic HF calculations. The accuracy of such calculations generally declines at both very small and very large  $r$ . To minimize the corresponding errors, it proved efficient to parametrize inner shells as hydrogenic and employ a nonuniform grid in  $r$ . For practical applications (e.g., for x-ray scattering), it is often sufficient to know only the radial electron densities, which may thus be reparametrized directly, provided this does not add significant errors at small  $r$ . An improved HF parametrization of that kind was proposed in [20]. It employs five exponential terms for the electron density (rather than for the screening function), automatically fulfilling (8), and is subjected to a few additional constraints, such as (10) and the equality of  $\langle r^2 \rangle$  to the appropriate atomic values. Some of the coefficients of the exponentials obtained by the fitting are negative. The resulting parametrization was assessed to be accurate up to reciprocal lattice vectors  $g = 12 \text{ \AA}^{-1}$ , improving the accuracy of older parametrizations [21], which held only up to  $g = 6 \text{ \AA}^{-1}$ . However, five exponentials may still not be enough to capture all the numerous shell features in a high- $Z$  atom. Caution is thus needed when different shells can contribute at simultaneously large  $Z$  and small  $r$  (large  $q$ ). In the discussion

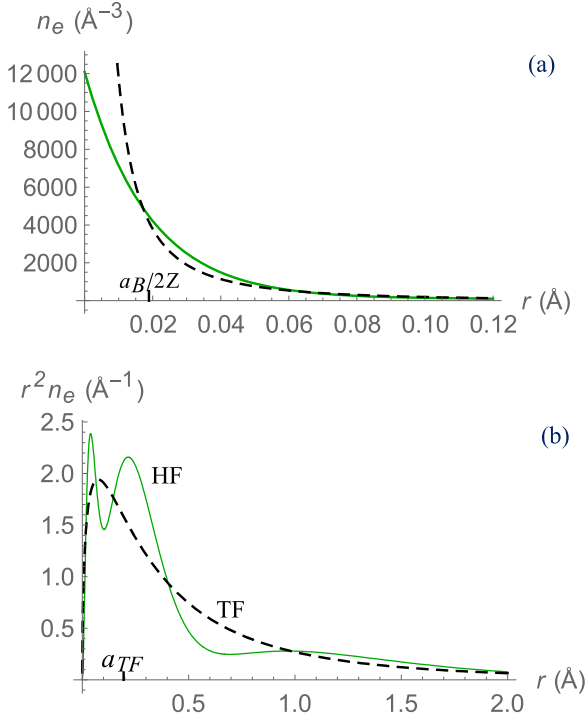


FIG. 2. Electron density in a silicon atom ( $Z = 14$ ). Green solid curves correspond to the HF density [20] and black dashed curves to the TF approximation. (a) The  $K$ -shell region, in which the density  $n_e(r)$  monotonically decreases. The  $K$ -shell radius equals  $a_B/2Z$  [see Eq. (81) below]. (b) Radial density  $r^2 n_e(r)$  in the full range, exhibiting three ( $K$ ,  $L$ , and  $M$ ) shells in a silicon atom. The integrals under both curves equal  $Z/4\pi$ . The TF radius  $a_{TF}$  for the given  $Z$  is evaluated by Eq. (14).

of mixed large- and moderate- $q$  physics in Sec. V, we will restrict ourselves to using the HF tables only for  $Z < 18$ .

A comparison of parametrization [20] with the TF approximation for the silicon atom is shown in Fig. 2. The HF density (solid curves) exhibits significant oscillatory deflections from the TF one (dashed curves), which is a manifestation of shell effects. It is thus evident that the TF approximation is rather crude, but as was noted in the Introduction, for semiclassical scattering problems, shell contributions are often smeared out by averaging along the particle trajectory as well as over its impact parameters. This smearing is what we wish to quantify next.

### B. Classical small-angle scattering in a screened Coulomb field

Turning to the description of scattering, we restrict our attention to the high-energy case, which is the least obscured and complicated by dynamical effects. At the same time, in spite of the high momentum, heavy projectiles such as protons and ions may have a moderate velocity (a condition to be specified later in Sec. II C 1), making their atomic scattering amenable to classical treatment [1, 22, 23]. The classical description of scattering depends on fewer parameters (not involving the Planck constant) and promises to be simpler. We thus treat the classical case first.

Consider a beam of energetic pointlike charged particles (protons or bare nuclei with a charge  $Z_1 e$ ) incident on an

atom with a velocity  $v$  along the  $z$  axis. In the leading-order high-energy approximation, the (predominantly transverse to  $z$  axis) momentum transferred to a fast classical particle at an impact parameter  $\mathbf{b}$  is expressed as a derivative

$$\mathbf{q}(\mathbf{b}) = \frac{\partial}{\partial \mathbf{b}} \chi_0(\mathbf{b}) \quad (19)$$

of the function [16, 23, 24]

$$\chi_0(\mathbf{b}) = -\frac{Z_1 e}{v} \int_{-\infty}^{\infty} dz \varphi(z, \mathbf{b}), \quad (20)$$

where  $\varphi$  is the electrostatic potential (1) of the atom. This function carries all the information about the atomic potential required for description of high-energy scattering. It arises also in the quantum-mechanical description (see Sec. II C), where it amounts to an eikonal phase in units of  $\hbar$ .

The function  $\chi_0(\mathbf{b})$ , in which the longitudinal coordinate of the atomic potential is integrated out, obeys a Laplace equation in the transverse plane

$$\begin{aligned} \Delta_{\perp} \chi_0(\mathbf{b}) &= -\frac{Z_1 e}{v} \int_{-\infty}^{\infty} dz \Delta \varphi(z, \mathbf{b}) \\ &= 4\pi \frac{Z_1 e^2}{v} \left( Z \delta(\mathbf{b}) - \int_{-\infty}^{\infty} dz n_e(z, \mathbf{b}) \right) \end{aligned} \quad (21)$$

involving the projected electron density  $\int_{-\infty}^{\infty} dz n_e(z, \mathbf{b})$ . From this equation,  $\chi_0(\mathbf{b})$  may be evaluated directly, bypassing evaluation of  $\varphi$ . In the  $b \rightarrow 0$  limit, the right-hand side of (21) is dominated by the  $\delta$ -function term (the atomic nucleus contribution). Taking into account the identity  $\Delta_{\perp} \ln b = 2\pi \delta(\mathbf{b})$ , the small- $b$  asymptotics of  $\chi_0$  follows in the form

$$\chi_0(\mathbf{b}) \underset{b \rightarrow 0}{\simeq} \frac{2Z_1 Z e^2}{v} \ln \frac{b}{b_0}. \quad (22)$$

The constant  $b_0$  under the logarithm will be determined later, in Sec. II C.

#### 1. Expression for the indicatrix in terms of $n_e(r)$

For our calculations of shell effects in classical scattering it will be instrumental to reduce the scattering indicatrix  $q(b)$  to a *single* integral of the electron spatial distribution  $n_e(r)$ , on account of the spherical symmetry of the latter. Rewrite Eq. (21) for  $b > 0$  as

$$\begin{aligned} \frac{1}{b} \frac{\partial}{\partial b} b q &= \frac{1}{b} \frac{\partial}{\partial b} b \frac{\partial}{\partial b} \chi_0 \equiv \Delta_{\perp} \chi_0 \\ &= -4\pi \frac{Z_1 e^2}{v} \int_{-\infty}^{\infty} dz n_e(z, b). \end{aligned}$$

Multiplication of both sides by  $b$  and integration over  $b$  taking into account the boundary condition  $q(\infty) = 0$  produces a double-integral expression of  $q$  through  $n_e(r)$ . It may be cast in a factorized form

$$q(b) = \frac{2Z_1 Z e^2}{vb} S_1(b), \quad (23)$$

with

$$Z S_1(b) = 2\pi \int_b^{\infty} db' b' \int_{-\infty}^{\infty} dz n_e(b', z) \quad (24)$$

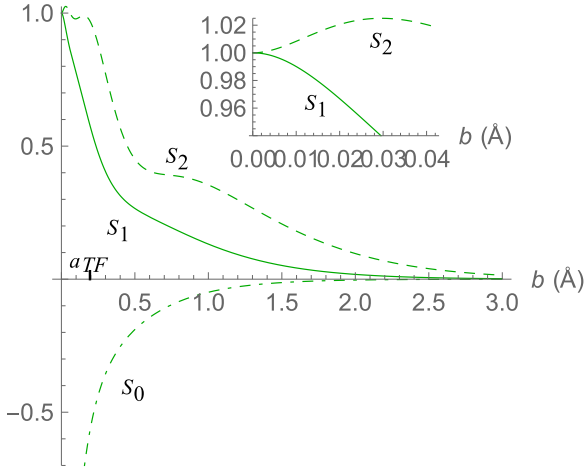


FIG. 3. Functions  $S_1(b)$  [Eq. (25)],  $S_2(b)$  [Eq. (32)], and  $S_0(b)$  [Eq. (44)], evaluated using HF electron densities [20] for a silicon atom. Due to the averaging over the projectile trajectory, the shell structure in them is less pronounced than in the electron density [cf. Fig. 2(b)]. The inset shows the behavior of  $S_1(b)$  and  $S_2(b)$  in the small- $b$  region.

being nothing but the number of electrons outside a cylinder of radius  $b$ . (This number is proportional to the total electric charge contained within that cylinder, which, due to the axial symmetry and Gauss's divergence theorem, for a neutral atom unambiguously determines the mean transverse radial electric-field strength at a given  $b$ .) Passage to spherical coordinates allows one to accomplish all the integrations except the radial one, involving the atom-dependent function  $n_e(r)$ :

$$S_1(b) = \frac{4\pi}{Z} \int_b^\infty dr r \sqrt{r^2 - b^2} n_e(r) \quad (25a)$$

$$\equiv \frac{2\pi}{Z} \int_{-\infty}^\infty dz z^2 n_e(r)|_{r=\sqrt{b^2+z^2}}. \quad (25b)$$

Observing that

$$S_1(0) = \frac{1}{Z} \int d^3r n_e(r) = 1,$$

from Eq. (23) one verifies that large-momentum-transfer scattering asymptotics  $q(b) \underset{b \rightarrow 0}{\simeq} \frac{2Z_1 Z e^2}{vb}$  is screening independent and complies with (22). The behavior of the function  $S_1(b)$  for a silicon atom is illustrated in Fig. 3. It is much smoother than the underlying  $r^2 n_e(r)$  shown in Fig. 2(b). This bears out the averaging effect mentioned in the Introduction. Now it is quantified by Eqs. (24) and (25).

The classical differential cross section  $d\sigma_{\text{cl}}/d^2q$  is next obtained by differentiation (evaluation of a Jacobian) of the impact parameters by momentum transfers or, conversely, of momentum transfers by impact parameters. The latter may be done directly, given the indicatrix (23) and (25a):

$$\frac{d\sigma_{\text{cl}}}{d^2q} = \left| \frac{\partial \mathbf{b}}{\partial \mathbf{q}} \right| = \left| \frac{\partial \mathbf{q}}{\partial \mathbf{b}} \right|^{-1} = \left| \det \frac{\partial^2 \chi_0}{\partial b_i \partial b_k} \right|^{-1}. \quad (26)$$

To express the differential cross section in terms of the momentum transfer, one needs yet to express  $b$  through  $q$ .

Equation (23) in its generic form is not invertible explicitly but can serve to relate  $d\sigma$  and  $q$  parametrically.

In the present high-energy approximation, obviously there is no  $Z_1$  charge sign (or, equivalently,  $q$  sign) dependence. In fact, the dependence on the charge absolute value in classical mechanics can be eliminated as well, as is shown below.

## 2. The $Z_1/v$ scaling for the classical momentum transfer

In what follows, it will be more convenient to compare the relative than absolute cross sections. Also, since in Eqs. (20), (21), and (23) the momentum transfer is proportional to the particle charge  $Z_1$  and is reciprocal to the particle velocity, the dependence of  $d\sigma_{\text{cl}}/d^2q$  on these parameters can be eliminated by passing to a reduced variable

$$Q(b) = \frac{v}{2Z_1 Z e^2} q(b) \quad (27a)$$

$$= \frac{1}{b} S_1(b). \quad (27b)$$

The latter depends only on  $b$  and implicitly on  $Z$ , but not on  $Z_1/v$ .

To recast the differential cross section in terms of the reduced momentum  $Q$ , it suffices to multiply (26) by  $q^2$ , counterweighting the  $q^2$  scale in  $d^2q$  in the denominator:

$$q^2 \frac{d\sigma_{\text{cl}}}{d^2q} = Q^2 \frac{d\sigma_{\text{cl}}}{d^2Q} = Q^2 \left| \frac{\partial Q}{\partial \mathbf{b}} \right|^{-1} = Q^2 \left| \frac{db^2}{dQ^2} \right|. \quad (28)$$

The advantage of such a product is that it, besides  $Z$ , depends only on  $b$  or on  $Q(b)$ , but not on  $q(b)$  and  $Z_1/v$  independently. Even more convenient is to work with the ratio  $d\sigma_{\text{cl}}/d\sigma_{\text{R}}$ , where

$$q^2 \frac{d\sigma_{\text{cl}}}{d^2q} \equiv Q^2 \frac{d\sigma_{\text{cl}}}{d^2Q} = Q^{-2} \quad (29)$$

is the Rutherford cross section for the unscreened Coulomb field, obtained by substituting  $Q = 1/b$  into (28). The ratio  $d\sigma_{\text{cl}}/d\sigma_{\text{R}}$  tends to unity at large  $Q$ , and for the same reason as for (28), depends only on  $Z$  and  $Q$ :

$$\frac{d\sigma_{\text{cl}}}{d\sigma_{\text{R}}} = Q^4 \frac{d\sigma_{\text{cl}}}{d^2Q} = Q^4 \left| \frac{db^2}{dQ^2} \right| = \mathcal{R}(Z, Q), \quad (30)$$

$$\mathcal{R}(Z, 0) = 0, \quad \mathcal{R}(Z, \infty) = 1.$$

On inserting (27b) and (25a) into Eq. (30) and evaluating the derivative, we arrive at a representation

$$\frac{d\sigma_{\text{cl}}}{d\sigma_{\text{R}}} = \frac{S_1^3(b)}{b^2 |dQ/db|} = \frac{S_1^3(b)}{S_2(b)}. \quad (31)$$

The denominator here involves a new function  $S_2$  related to  $S_1$  by differentiation:

$$S_2(b) = \frac{dQ}{d(1/b)} = \left( 1 - b \frac{d}{db} \right) S_1(b) \quad (32a)$$

$$= \frac{4\pi}{Z} \int_b^\infty \frac{dr r^3}{\sqrt{r^2 - b^2}} n_e(r) \quad (32b)$$

$$= \frac{2\pi}{Z} \int_{-\infty}^\infty dz r^2 n_e(r)|_{r=\sqrt{b^2+z^2}}. \quad (32c)$$

Like  $S_1(b)$ , it equals unity in the origin:

$$S_2(0) = \frac{1}{Z} \int d^3r n_e(r) = 1.$$

The behavior of the function  $S_2(b)$  for a silicon atom is illustrated in Fig. 3 by the dashed curve. Notably, compared with  $S_1(b)$ , it manifests stronger shell effects. That may be traced to the  $S'_1(b)$  term in Eq. (32a), which eliminates the  $b$  integration in the representation (24), or to a more singular integrand in Eq. (32b), making the relationship with  $n_e(r)$  more local. Equation (31), through (25a) and (32b), and Eq. (27b) define a parametric dependence (with  $b$  the parameter) of  $d\sigma_{cl}/d\sigma_R$  on  $Q$ .

### 3. Thomas-Fermi scaling in classical scattering

As long as shell effects in the  $q$  dependence of the classical scattering cross section are milder than for  $r^2 n_e(r)$ , for its description it is tempting to combine the classical scaling with that existing in the TF model. Substitution of (18) and (16) into (27b), (25a), and (32b) leads to a parametric dependence of the differential cross section

$$\frac{d\sigma_{cl}^{TF}}{d\sigma_R} = \mathcal{R}_{TF}(a_{TF}Q) = \frac{[S_1^{TF}(B)]^3}{S_2^{TF}(B)} \quad (33)$$

and the reduced momentum transfer

$$Q(B) = \frac{1}{a_{TF}(Z)B} S_1^{TF}(B) \quad (34)$$

on the impact parameter in units of the Thomas-Fermi radius,

$$B(Z, b) = \frac{b}{a_{TF}(Z)}. \quad (35)$$

The functions  $S_{1,2}^{TF}$  are expressed through the TF screening function via

$$S_1^{TF}(B) = \int_B^\infty d\xi \sqrt{\xi - \frac{B^2}{\xi}} \phi_{TF}^{3/2}(\xi), \quad (36)$$

$$S_2^{TF}(B) = \int_B^\infty \frac{d\xi \xi}{\sqrt{\xi - B^2/\xi}} \phi_{TF}^{3/2}(\xi). \quad (37)$$

They are shown in Fig. 4 by the solid and the dashed curve, respectively. Compared with HF functions exemplified in Fig. 3, their behavior is smoother.

The differential cross section of classical scattering on a TF atom, defined by Eqs. (33)–(37), is plotted in Fig. 5 by the dashed curve. At moderately low  $a_{TF}Q$ , visually, it rises approximately linearly [cf. Eq. (8) in [25] and Eq. (6.64) in [26]]:

$$\frac{d\sigma_{cl}^{TF}}{d\sigma_R} \underset{0.1 \lesssim a_{TF}Q \lesssim 1}{\simeq} 0.415 a_{TF}Q. \quad (38)$$

At very low  $a_{TF}Q$  (see the inset of Fig. 5), the ratio  $\frac{1}{a_{TF}Q} \frac{d\sigma_{cl}^{TF}}{d\sigma_R}$  actually tends not to 0.415 but to zero.<sup>1</sup> Such a

<sup>1</sup>According to Eqs. (33) and (34),  $\frac{1}{a_{TF}Q} \frac{d\sigma_{cl}^{TF}}{d\sigma_R} = \frac{B(S_1^{TF})^2}{S_2^{TF}}$ . This expression tends to zero both at  $B \rightarrow 0$  ( $Q \rightarrow \infty$ ) and at  $B \rightarrow \infty$  ( $Q \rightarrow 0$ ), since  $S_1^{TF}(B) \sim S_2^{TF}(B) \sim B^{-3}$ .

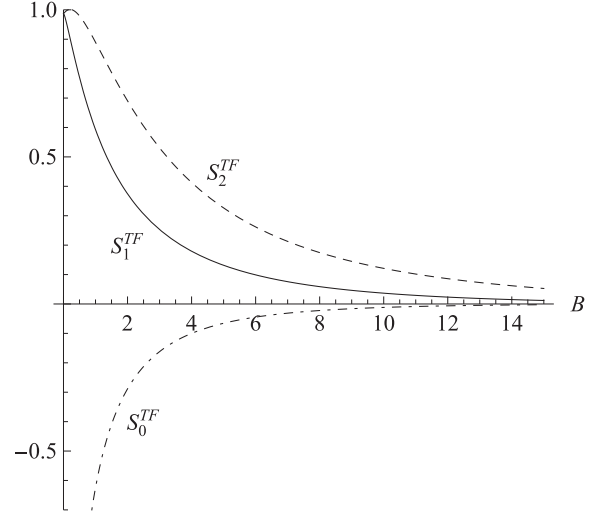


FIG. 4. Functions  $S_1^{TF}(B)$  [Eq. (36)],  $S_2^{TF}(B)$  [Eq. (37)], and  $S_0^{TF}(B)$  [Eq. (53)].

ratio was investigated in [27], where it was denoted by  $f(\eta)$ , with  $\eta = a_{TF}Q/2$ .<sup>2</sup> The coefficient 0.415 in the formula (38) approximately corresponds to the maximum of the Lindhard-Nielsen-Scharff function  $f$ . For scattering in solids, the extensibility of this function far below its maximum may be unreliable, so long as the TF approximation breaks down at  $\xi > 10$ , yet outer shells are generally distorted by the formation of interatomic bonds. However, the maximum corresponds to rather typical  $Q$ .

### 4. Comparison with the HF-based cross section

We are now in a position to compare the scattering differential cross section in the TF approximation with that evaluated by (31) with HF electron densities [20]. The results, for exemplary values  $Z = 3$  and 14, are shown in Fig. 5. For classical scattering (in contrast to quantum, which will be treated in the next section), no pronounced oscillatory effects in  $Q$  dependences are observed. That is natural because, as was pointed out above, transverse and longitudinal spatial integrations largely smear out the multippeak structure of  $r^2 n_e(r)$ .

Nonetheless, some differences between HF and TF scattering cross sections are manifest. If  $Z$  is low, the HF and TF results do not coincide for any  $Q$  except at a single crossing point. If  $Z$  is high, the HF and TF results coalesce at moderate  $a_{TF}Q$ , but at high  $a_{TF}Q$  they split apart, although not as rapidly as for low  $Z$ .

This demonstrates that for sufficiently large  $Z$  the accuracy of the TF approximation for  $d\sigma_{cl}/d\sigma_R$  can be satisfactory, but only for limited momentum transfers (e.g.,  $a_{TF}Q < 6$  for  $Z = 14$  in Fig. 5). For larger  $a_{TF}Q$  it does not describe the deviation of  $d\sigma_{cl}/d\sigma_R$  from unity adequately. This is chained to the fact that, as was mentioned in Sec. II A 2, the TF

<sup>2</sup>At the small scattering angles considered here,  $Q$  corresponds to the Lindhard-Nielsen-Scharff variable  $t^{1/2}$  [27].

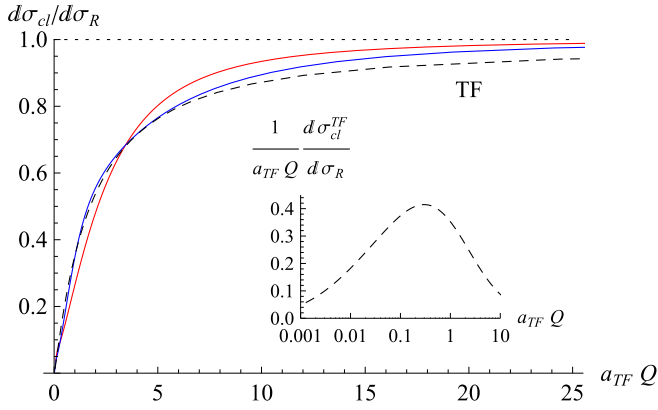


FIG. 5. Ratio of the classical scattering differential cross section to its Rutherford asymptotics. The black dashed curve shows  $d\sigma_{cl}^{TF}/d\sigma_R$  calculated for the TF approximation of the atomic electron density [Eqs. (33)–(37)]. The solid curves show the ratio  $d\sigma_{cl}/d\sigma_R$  calculated by Eqs. (31), (25a), and (32b) with  $n_e(r)$  from HF tables [20] for  $Z = 3$  (Li), red curve, and  $Z = 14$  (Si), blue curve. For each  $Z$ ,  $a_{TF}(Z)$  is evaluated by Eq. (14). For  $Z = 14$ , the result for  $d\sigma_{cl}/d\sigma_R$  is closer to the TF prediction, virtually coinciding with it at  $a_{TF} Q < 6$ . The deviation from TF for  $a_{TF} Q > 6$  is predominantly determined by inner shells. The inset shows the behavior of the slope  $\frac{1}{a_{TF} Q} \frac{d\sigma_{cl}^{TF}}{d\sigma_R}$  at very low  $a_{TF} Q$ , reaching a maximum, and tending to zero at both sides away from it.

approximation breaks down at small  $r$ , which is responsible for large momentum transfers.

The differences from the TF approximation observed in the hard-scattering region deserve a more detailed investigation, and their relationship with inner shells is plausible. That will be the object of our study in Sec. IV. Meanwhile, we will extend our treatment to the quantum domain.

### C. Quantum (eikonal) scattering in a screened Coulomb potential

At high energy, atomic scattering is sufficiently simple to treat quantum mechanically too, because quantum transverse motion, just like classical, is suppressed by an inverse power of the large longitudinal momentum [2,16,23,28]. Exchange amplitudes between the incident fast electron and atomic electrons are negligible. (If the projectile is a proton or a bare nucleus, exchange channels are completely absent.) Therefore, to the leading order in energy, the scattering is governed by the mean electrostatic potential of the nucleus and its bound electrons.

The negligibility of quantum transverse motion within the atomic field action domain implies that the particle wave function at a given impact parameter virtually does not depend on the wave-function values at other impact parameters. It just gains a position-dependent phase factor, which tends to a finite limiting value  $e^{(i/\hbar)\chi_0(b)}$  behind the atom. The eikonal phase  $\chi_0(b)$  here is the same as the formerly encountered function (20). At large distances behind the atom, however, wave properties of the transverse motion ultimately unfreeze, giving rise to diffraction. The amplitude  $a$  of scattering with

a definite  $q$  (or deflection angle) thus receives interfering contributions from all the impact parameters, in accordance with the Huygens principle:

$$a(q) = \frac{1}{2\pi i\hbar} \int d^2b e^{(i/\hbar)\mathbf{q}\cdot\mathbf{b}} (1 - e^{(i/\hbar)\chi_0(b)}). \quad (39)$$

The differential scattering cross section for this so-called eikonal approximation [2,16,23,28] is expressed as

$$\frac{d\sigma}{d^2q} = |a|^2. \quad (40)$$

#### 1. Integral representation of the eikonal phase through $n_e(r)$

Similarly to Sec. II B, we factorize the exponent in (39) as

$$i \frac{\chi_0(b)}{\hbar} = 2i\alpha S_0(b), \quad (41)$$

extracting all the dependence on  $Z_1$  and  $v$  to a prefactor

$$\alpha = \frac{Z_1 Z e^2}{\hbar v} \quad (42)$$

known as the Coulomb parameter. The isolated atom-specific factor

$$S_0(b) = - \int_b^\infty db' Q(b') \equiv - \int_b^\infty \frac{db'}{b'} S_1(b') \quad (43)$$

depends on only  $b$  and  $Z$ . By inserting here the representation (25a) for  $S_1(b)$ , changing the integration order, and doing the  $b'$  integration, one is led to a single-integral expression for  $S_0$  through  $n_e(r)$ :

$$S_0(b) = \frac{4\pi}{Z} \int_b^\infty dr r \left( \sqrt{r^2 - b^2} - r \operatorname{arccosh} \frac{r}{b} \right) n_e(r). \quad (44)$$

The function  $S_0(b)$  is everywhere negative and diverges at small  $b$  logarithmically,

$$S_0(b) \underset{b \rightarrow 0}{\simeq} \ln \frac{b}{b_0}, \quad (45)$$

complying with Eq. (22) (see the dot-dashed curve in Fig. 3). An explicit integral representation (44), in which the  $b$ -dependent block in the integrand asymptotically behaves logarithmically, as

$$\sqrt{r^2 - b^2} - r \operatorname{arccosh} \frac{r}{b} \underset{b \rightarrow 0}{\simeq} r \left( 1 - \ln \frac{2r}{b} \right),$$

enables one to infer the constant  $b_0$ , which appeared in Eq. (22):

$$\ln b_0 = \langle \ln 2r \rangle - 1. \quad (46)$$

We will adopt throughout the definition for atomic averaging of any function  $F(r)$  in the form

$$\langle F(r) \rangle = \frac{4\pi}{Z} \int_0^\infty dr r^2 n_e(r) F(r), \quad (47)$$

including the  $1/Z$  prefactor, to satisfy the identity  $\langle 1 \rangle = 1$ .

At large  $q$ , the integral (39) is dominated by small- $b$  contributions. Therefore, high- $q$  asymptotics of the scattering

amplitude is obtained by inserting (45) in (39):

$$\begin{aligned} a \xrightarrow{q \rightarrow \infty} a_R &= b_0^{-2i\alpha} \frac{i}{2\pi\hbar} \int d^2b e^{(i/\hbar)\mathbf{q}\cdot\mathbf{b}} b^{2i\alpha} \\ &= b_0^{-2i\alpha} \frac{i}{\hbar} \int_0^\infty db b^{1+2i\alpha} J_0(qb/\hbar) \\ &= \frac{1}{qQ} \left( \frac{2\hbar}{qb_0} \right)^{2i\alpha} \frac{\Gamma(1+i\alpha)}{\Gamma(1-i\alpha)}. \end{aligned} \quad (48)$$

Note that although the phase of  $a_R$  depends nontrivially on the value of the Coulomb parameter  $\alpha$ , yet the global phase depends on the screening via  $b_0$ , in the differential cross section (40) those dependences drop out:

$$\frac{d\sigma_R}{d^2q} = |a_R|^2 = \frac{1}{q^2 Q^2}. \quad (49)$$

Therefore, Eq. (49) coincides with its classical counterpart (29). That is the salient feature of the Rutherford scattering.

At smaller momentum transfers, when the sensitivity of  $d\sigma/d^2q$  to screening is restored, the ratio  $d\sigma/d\sigma_R$  in general becomes  $\alpha$  dependent. However, if  $\alpha$  is large or small, the dependence on it fades away or becomes trivial so that  $d\sigma/d\sigma_R$  essentially reduces to a function of a single variable.

Specifically, if both  $Z_1$  and  $Z_2$  are large, or  $v \ll c$ , the parameter (42) can be large ( $\alpha \gtrsim 1$ ) despite that  $e^2/\hbar c = 1/137 \ll 1$ , viz., for scattering of protons on silicon ( $Z = 14$ ), the boundary between the perturbative and nonperturbative regimes lies at a collision energy of 5 MeV, when  $v \approx 0.1c$  and  $\alpha \approx 1$ . As  $\alpha \rightarrow \infty$ , evaluation of the integral

$$\frac{d\sigma}{d\sigma_R} = \left| \frac{i}{2\alpha} \frac{q^2}{\hbar^2} \int_0^\infty db b J_0(qb/\hbar) (e^{2i\alpha S_0(b)} - 1) \right|^2 \quad (50)$$

in the stationary-phase approximation leads back to (31):

$$\frac{d\sigma}{d\sigma_R} \xrightarrow{\alpha \rightarrow \infty} \frac{d\sigma_{cl}}{d\sigma_R}.$$

In this limit, the cross-section ratio depends on  $q$ ,  $Z_1$ , and  $v$  only through a single variable  $Q$ . The semiclassical atomic scattering regime and its applications are discussed in [22,23].

In the opposite limit  $|\alpha| \ll 1$  [e.g., for  $|Z_1| = 1$  (initial electron or proton), not too high an atomic number of the target  $Z_2 \ll \hbar c/e^2 = 137$ , and relativistic projectile velocities  $v \sim c$ ], the exponential in (50) may be linearized:

$$\frac{d\sigma}{d\sigma_R} \xrightarrow{\alpha \rightarrow 0} \frac{d\sigma_1}{d\sigma_R} = \left| \frac{q^2}{\hbar^2} \int_0^\infty db b J_0(qb/\hbar) S_0(b) \right|^2.$$

It depends only on  $q/\hbar = 2\alpha Q$ . On inserting here (44) and utilizing the integral

$$\int_0^r db b J_0(kb) \left( \sqrt{r^2 - b^2} - r \operatorname{arccosh} \frac{b}{r} \right) = \frac{\sin kr - kr}{k^3},$$

one retrieves the familiar form factor formula [2,29,30]

$$\frac{d\sigma_1}{d\sigma_R} = [1 - \Phi(q)]^2, \quad (51)$$

where

$$\Phi(q) = \frac{4\pi}{Z} \int_0^\infty dr r^2 \frac{\sin qr/\hbar}{qr/\hbar} n_e(r) \equiv \frac{1}{Z} \int d^3r e^{i\mathbf{q}\cdot\mathbf{r}/\hbar} n_e(r) \quad (52)$$

is the atomic form factor.

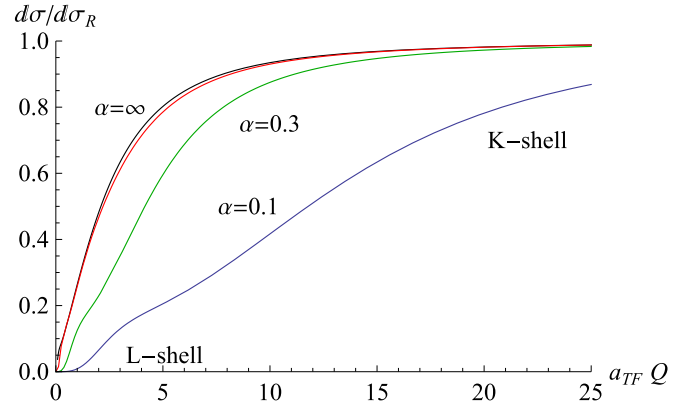


FIG. 6. Differential scattering cross-section ratios relative to the Rutherford cross section vs the reduced momentum transfer in units of the inverse TF radius, for scattering on a lithium atom ( $Z = 3$ ). The curves correspond to  $\alpha = 0.1$  (blue), 0.3 (green), and 1 (red). For  $\alpha = 1$ , the cross-section ratio nearly coincides with its classical limit shown by the black curve (corresponding to the red curve in Fig. 5). At small  $\alpha$ , there are noticeable shell effects: *K*-shell and *L*-shell contributions manifest as shallow bulges.

In the TF approximation (18) and (13), the function (44) becomes

$$S_0^{\text{TF}}(B) = S_1^{\text{TF}}(B) - \int_B^\infty d\xi \sqrt{\xi} \operatorname{arccosh} \frac{\xi}{B} \phi_{\text{TF}}^{3/2}(\xi), \quad (53)$$

where  $S_1^{\text{TF}}(B)$  is given by Eq. (36) and  $B$  is related to  $b$  by Eq. (35).

## 2. Eikonal scattering on Hartree-Fock atoms

In Figs. 6 and 7 the quantum cross-section ratio  $d\sigma/d\sigma_R$  is plotted for exemplary atomic numbers  $Z = 3$  and 14, for several values of Coulomb parameter  $\alpha$ . The limit  $\alpha \rightarrow \infty$  (black curves) corresponds to the semiclassical approximation, in

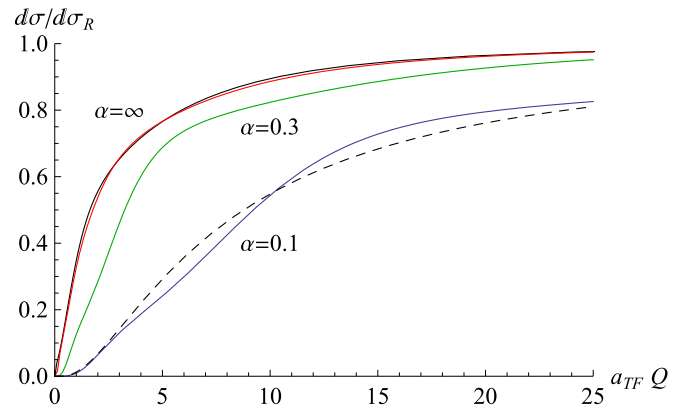


FIG. 7. Same as in Fig. 6 but for scattering on a silicon atom ( $Z = 14$ ). The curves correspond to  $\alpha = 0.1$  (blue), 0.3 (green), and 1 (red). For  $\alpha = 1$ , the ratio nearly coincides with its classical limit (the blue curve in Fig. 5). For small  $\alpha$ , the shape of the  $Q$  dependence is different from classical (the black curve), but shell effects are faint. The black dashed curve shows the TF form factor [Eqs. (51) and (18)] for  $\alpha = 0.1$ .

which  $d\sigma/d\sigma_R$  depends on the single variable  $Q$ . At  $\alpha = 1$  (red curves in Figs. 6 and 7), for any  $Z$ , the cross section is already fairly close to classical. By contrast, at  $\alpha = 0.1$  (blue curves in Figs. 6 and 7), it is well approximated by the form factor formula (51) and exhibits shell effects provided  $Z$  is not too large (Fig. 6) [in contrast to  $r^2 n_e(r)$ , for which shell effects are prominent even at high  $Z$ ]. There it depends virtually on a single variable  $q/\hbar = 2\alpha Q$ .

This gives a basic idea of the  $q$  dependence of  $d\sigma/d\sigma_R$  in the entire range of momentum transfers and for any value of the Coulomb parameter. The only variable, the dependence on which has not been explored in detail yet, is the target atomic number  $Z$ . It is not ruled out that shell effects in this dependence can actually be more pronounced than in the  $q$  dependence. We will investigate the  $Z$  dependence in what follows and show that this is indeed the case. To reasonably restrict our consideration, we will focus on just a few representative numbers characterizing the single-scattering differential cross section at moderate and large momentum transfers and also on the Molière screening angle, which characterizes multiple scattering.

### III. SHELL EFFECTS IN CLASSICAL ATOMIC SCATTERING AT MODERATE MOMENTUM TRANSFERS

At typical moderate  $q$  the scattering cross section generally behaves in a complicated manner, as was illustrated above in Figs. 6 and 7. In the classical case, however, the behavior of  $d\sigma_{cl}/d\sigma_R$  at moderate  $Q$  ( $a_{TF}Q \lesssim 1$ ) is characterized primarily by its slope. As has been pointed out for the two exemplary cases in Fig. 5, this slope can appreciably differ from the corresponding TF prediction, especially at low  $Z$ . Since, according to Eqs. (31), (25a), (32b), and (27b), moderate  $Q$  corresponds to moderate  $b$ , this deviation may generally be expected to stem from outer- or intermediate-shell contributions. Such shells are not hydrogenic, so their description is less trivial than that for inner ones.

The most reliable way to evaluate the  $Z$  dependence of the mentioned slope is numerical. It will be easier to calculate this slope not as a derivative, but as the ratio  $\frac{1}{a_{TF}Q} \frac{d\sigma_{cl}}{d\sigma_R}$  at some suitable point in the region of linear behavior of  $d\sigma_{cl}/d\sigma_R$ . The only special point in this region is at the maximum of the slope

$$a_{TF}Q = 0.3, \quad (54)$$

corresponding to  $B = 1.53$  (see the inset of Fig. 5). In Fig. 8 the solid curve shows the  $Z$  dependence of  $\frac{1}{a_{TF}Q} \frac{d\sigma_{cl}}{d\sigma_R} |_{a_{TF}Q=0.3}$ , evaluated by Eqs. (31), (25a), and (32b) with HF electron densities [20]. It exhibits smooth regular oscillations about the TF value  $\max f = \frac{1}{a_{TF}Q} \frac{d\sigma_{cl}^{TF}}{d\sigma_R} |_{a_{TF}Q=0.3} = 0.415$  (the dotted line). To understand the nature of these oscillations, it could be valuable to relate them to known regularities in the electronic structure of the atom.

First of all, it is suggestive to compare these oscillations with the periods of the chemical Periodic Table of Elements, each ending by a noble gas. Some of the noble gases, Ne ( $Z = 10$ ), Kr ( $Z = 36$ ), and Rn ( $Z = 86$ ), are observed to correspond approximately to the centers of the broad minima in Fig. 8, but other noble gases, Ar ( $Z = 18$ ) and Xe ( $Z = 54$ ),

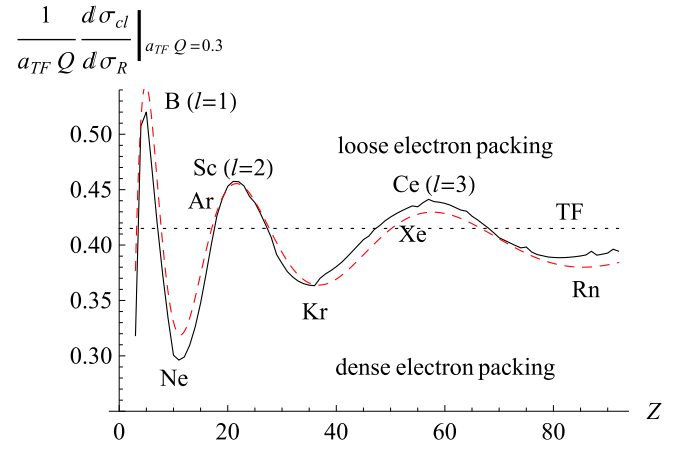


FIG. 8. The  $Z$  dependence of  $\frac{1}{a_{TF}Q} \frac{d\sigma_{cl}}{d\sigma_R}$  (the slope of the classical cross-section ratio) at its maximum,  $a_{TF}Q = 0.3$  (cf. Fig. 5). The black solid curve is evaluated based on HF densities [20]. The red dashed curve is a fit by parametrization (64). The black dotted is the corresponding (maximal) value of the Lindhard-Nielsen-Scharff function  $f = \frac{1}{a_{TF}Q} \frac{d\sigma_{cl}^{TF}}{d\sigma_R}$  (scattering on a TF potential) (cf. the inset of Fig. 5).

on the contrary, are close to the centers of the broad maxima. One extra maximum yet corresponds not to any noble gas but to Be ( $Z = 4$ ) and B ( $Z = 5$ ). It thus appears that chemistry (or first ionization energies) does not give a clue for the observed oscillatory behavior. That is not surprising, because chemical periods mainly reflect the structure of the outermost shell, containing a few electrons, whereas the projectile particle penetrates the entire atom.

However, the values of  $Z$ ,

$$\begin{aligned} Z = 5 \text{ (B, } l = 1), \quad Z = 21 \text{ (Sc, } l = 2), \\ Z = 58 \text{ (Ce, } l = 3), \end{aligned} \quad (55)$$

at which the maxima in Fig. 8 are achieved, correspond to the corners of the so-called left step or Janet variation of the Periodic Table [13,14]. This table in turn agrees with the phenomenological Madelung rule, asserting that electron ( $n, l$ ) shells are filled in order of increasing  $n + l$  rather than the principal quantum number  $n$  [14]. Every new shell that starts being filled is not necessarily the most peripheral. For instance, the largest  $d$  and  $f$  shells are often located inside the atom and do not participate in chemical reactions [10,12]. It should be admitted that to date, Madelung's rule has not been proven *ab initio* from quantum mechanics (Löwdin's challenge [14,31]), despite the continuing efforts [31–34].

The numbers (55) actually correspond to  $Z$  values at which a new value of  $l$  first appears. A physical explanation for them has been proposed, based on the TF potential [2,35]. It argues that for a screened Coulomb field, the centrifugal potential  $\frac{\hbar^2 l(l+1)}{2mr^2}$  for a given  $l$  dominates the electrostatic potential  $-Ze^2\phi_{TF}(\xi)/r$  not only at small, but also at large  $r$ . When it dominates for all  $r$  throughout, it precludes formation of a potential well. The condition at which a global minimum emerges in the effective potential  $V_{\text{eff}}(r) = V(r) + \frac{\hbar^2 l(l+1)}{2mr^2}$  (the sum of the electrostatic and the centrifugal potentials) is the simultaneous equality to zero of the effective potential and

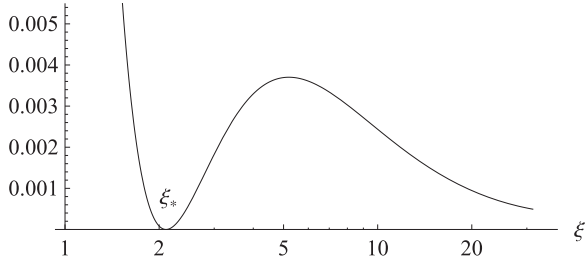


FIG. 9. Reduced effective potential  $\frac{a_{\text{TF}}}{Ze^2} V_{\text{eff}}(r) = -\frac{\phi_{\text{TF}}(\xi)}{\xi} + \frac{1}{2} \xi_* \phi_{\text{TF}}(\xi_*)$  of an electron with a definite angular momentum in the TF potential, for a value of  $Z$ , critical for the appearance of an orbital with an increased angular momentum. The value of  $\xi_*$ , the same for all  $l$ , is determined by Eq. (59).

of its derivative (see Fig. 9)

$$V_{\text{eff}}(r) = -\frac{Ze^2}{r} \phi_{\text{TF}}(\xi) + \frac{\hbar^2 l(l+1)}{2mr^2} = 0, \quad (56)$$

$$V'_{\text{eff}}(r) = 0. \quad (57)$$

By combining Eqs. (56) and (57), one can eliminate both  $Z$  and  $l$ :

$$\frac{d}{dr} [r^2 V_{\text{eff}}(r)] \propto \frac{d}{dr} [r \phi_{\text{TF}}(\xi)] \equiv \frac{d}{d\xi} [\xi \phi_{\text{TF}}(\xi)] = 0. \quad (58)$$

The latter equation has a single solution

$$\xi = \xi_* = 2.1, \quad (59)$$

at which point  $\xi_* \phi_{\text{TF}}(\xi_*) = 0.486$ . Note that the value (59) is comparable to a typical  $\xi$  contributing to (36) and (37) for  $B$  around 1.5 [see Eq. (54) and Fig. 10].

Once  $\xi$  is known, it is converted to  $r$  by Eqs. (13) and (14) and then  $Z$  is expressed from Eq. (56) as a function of  $l$ :

$$Z(l) = \frac{4}{3\pi} \left( \frac{l(l+1)}{\xi_* \phi_{\text{TF}}(\xi_*)} \right)^{3/2} = 1.25 [l(l+1)]^{3/2}. \quad (60)$$

The inversion of Eq. (60) gives for  $l(Z)$  in the argument of the cosine

$$2l(Z) = \sqrt{(Z/Z_0)^{2/3} + 1} - 1, \quad (61)$$

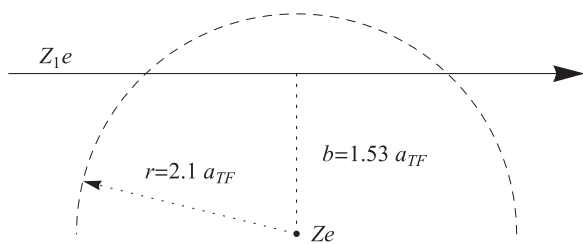


FIG. 10. Dashed circle corresponds to a radius  $r = \xi_* a_{\text{TF}}$ , with  $\xi_*$  given by Eq. (59), at which electron orbitals with a new momentum  $l$  first appear. The arrow shows the trajectory of a fast particle passage through an atom at an impact parameter  $b = 1.53 a_{\text{TF}}$ , corresponding to the largest slope of  $d\sigma_{\text{cl}}/d\sigma_{\text{R}}$  (the maximum of  $f$ ). A large part of the circle is close to the trajectory, making it plausible that the vicinity of the corresponding radius significantly contributes to the slope of  $d\sigma_{\text{cl}}/d\sigma_{\text{R}}$  at its maximum.

with  $Z_0 = 1.25 \times 4^{-3/2} = 0.156$ . Since  $Z_0 \ll 1$  and  $Z/Z_0 \gg 1$ , Eq. (61) may be approximated by

$$2l(Z) = (Z/Z_0)^{1/3} - 1, \quad (62)$$

which is equivalent to replacing in (56) and (60)  $l(l+1) \rightarrow (l+1/2)^2$ , as is usually done in the WKB approximation [2,35], in spite of  $l$  being not really large.

This derivation gives numbers (55) only approximately. Yet it does not take into account that an atomic electron, in contrast to the external projectile, moves in the potential [36]

$$-\frac{(Z-1)e^2}{r} \phi_{\text{TF}}(\xi) - \frac{e^2}{r}, \quad (63)$$

rather than  $-\frac{Ze^2}{r} \phi_{\text{TF}}(\xi)$  in Eq. (56). The residual  $-e^2/r$  term in (63) does not permit the centrifugal potential to dominate at asymptotically high  $r$  and leads to the formation of a double well or a knee feature in the single-well effective potential [10].

Nonetheless, the presented analysis suggests that once a new  $l$  opens up, it permits the atom to get packed more densely and thereby lower its energy. In this way, as  $Z$  monotonically increases, the atom size “breathes” with respect to its TF approximation. In application to scattering, denser packed (contracted) atoms correspond to smaller cross sections of scattering on them and to greater typical momentum transfers, i.e., to the minima in Fig. 8. Conversely, more loosely packed (swelled) atoms correspond to the maxima in Fig. 8.

A partial corroboration to this conjecture comes already from Fig. 2(b), where for  $Z = 14$  (belonging to the region of  $Z$  marked in Fig. 8 as denser packed) the HF distribution is indeed more compact than the TF one. To check this viewpoint further, in Fig. 11 we plot  $r^2 n_e(r)$ , best characterizing simultaneously the integrands of Eqs. (25) and (32), for the atoms corresponding to the maxima of Fig. 8 (left column) and to its minimum (right column), in the region  $r < 3a_{\text{TF}}$  relevant for the characteristic trajectory schematized in Fig. 10. Apparently, the distributions on the left are narrower than those on the right, because as  $Z$  increases, the shell maxima slide inside with respect to the TF distribution maximum and to the  $B$  value taken in Eq. (54). That also demonstrates why the oscillations of the slope of  $d\sigma_{\text{cl}}/d\sigma_{\text{R}}$  are so large, being about half the relative magnitude of oscillations in the  $r$  dependence of  $r^2 n_e$  in Fig. 2(b), despite being largely smeared out in the  $q$  dependence. So, alternating variations of the atom size do exist, whatever the explanation for their phase in terms of the shell buildup process; however, will not investigate the phase issue here in more detail.

To accomplish the phenomenological study of  $Z$  oscillations in the present problem, it may be expedient to approximate the oscillatory part of the  $\frac{1}{a_{\text{TF}} Q} \frac{d\sigma_{\text{cl}}}{d\sigma_{\text{R}}}$  dependence on  $Z$  by a simple trigonometric function times a power law:

$$\frac{1}{a_{\text{TF}} Q} \frac{d\sigma_{\text{cl}}}{d\sigma_{\text{R}}} = C_0 \left( 1 + \frac{A_0}{Z^\mu} \cos[2\pi l(Z) + \alpha_0] \right). \quad (64)$$

When employing (61) in (64), because the values (60) are somewhat lower than empirical ones (55), it is more accurate to treat  $Z_0$  as a fitting parameter, along with  $C_0$ ,  $A_0$ ,  $\alpha_0$ , and  $\mu$ . The fit of the ansatz (64) to the data (the red dashed curve in Fig. 8) gives  $C_0 \approx 0.4$ ,  $A_0 \approx 1$ ,  $\mu \approx \frac{2}{3}$ ,  $Z_0 \approx 0.14$ ,

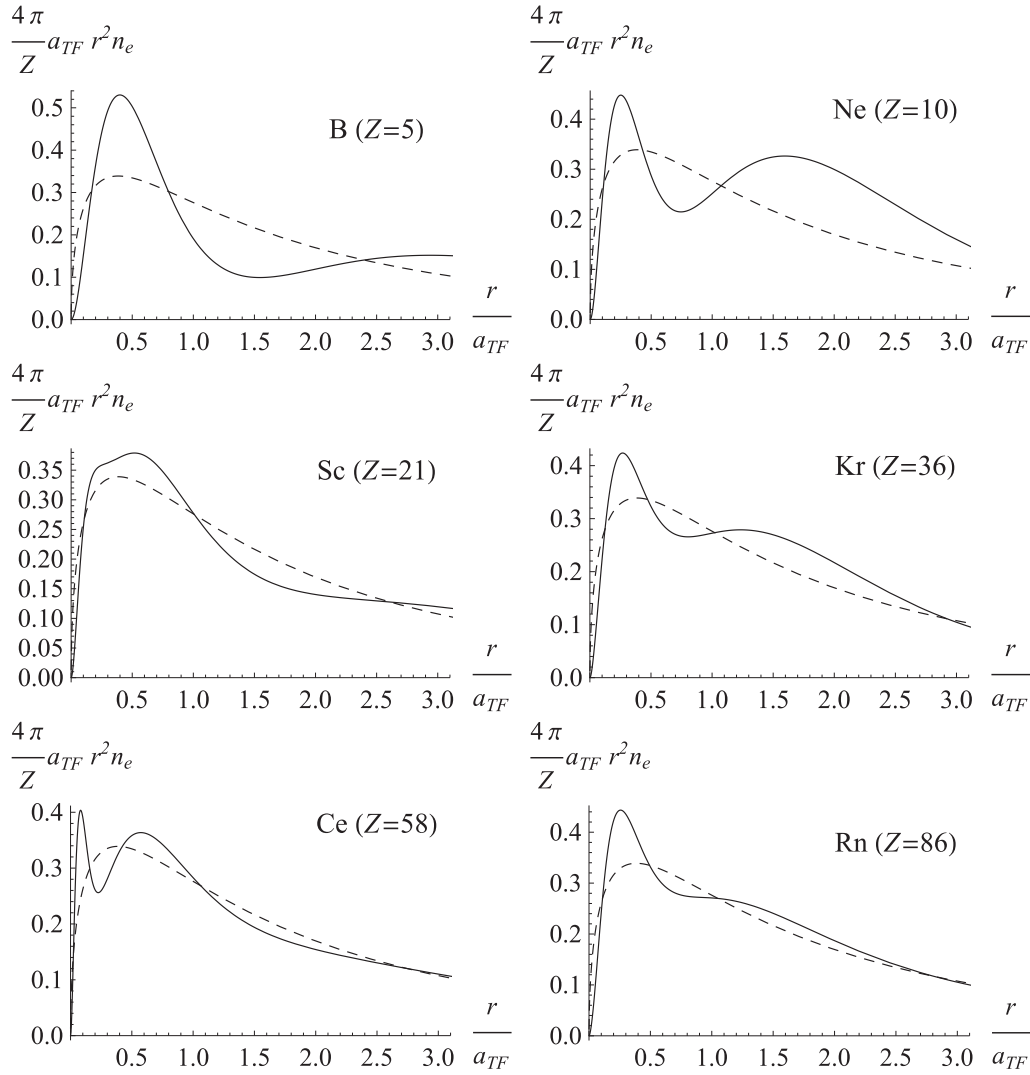


FIG. 11. Radial density distributions vs  $\xi = r/a_{TF}$  for atoms corresponding to the maxima of Fig. 8 (left column) and those corresponding to its minima (right column). Dashed curves show the  $Z$ -independent TF distribution.

and  $\alpha_0 \approx 1.4$ . Too much meaning should not be attached to the substantial additional phase  $\alpha_0 > 0$ : It just reflects the fact that the prefactor  $Z^{-\mu}$  shifts the locations of the extrema to the left.

We have thus described  $Z$  oscillations at a single value of  $Q$  only. Of course, similar oscillations take place for any  $Q \lesssim a_{TF}^{-1}$ , and it would be worth knowing how they depend on the  $Q$  value. Not contemplating here an exhaustive analysis, let us just mention that the form of (64) and (61) remains valid in a rather wide range of  $Q$ , but its parameters become  $Q$  dependent. In general, as  $Q$  increases, the amplitude  $A_0$  of the oscillations decreases.

Finally, it will be instructive to compare the oscillations of the slope of  $d\sigma_{cl}/d\sigma_R$  with  $Z^{1/3}$ -periodic dependences found in the literature for other observables. In [37] tiny (of relative magnitude  $\sim 10^{-3}$ ) oscillations with similar periodicity and phase were discussed for atomic total binding energies. There the power-law index of the oscillation envelope was twice higher,  $\mu \approx \frac{4}{3}$ , yet in [37] the maxima had a double-humped structure; an  $l$ -quantized TF model was developed to explain that.

A more significant  $Z^{1/3}$ -periodic dependence was found in [38] for quantum defects or phase shifts of zero-energy electron wave functions in atoms, taking into account the  $-e^2/r$  interaction at large  $r$  similar to that in Eq. (63). Those oscillations, more clearly displayed in [39], are less regular, but their phase does not contradict that in our Fig. 8.

Taking into account the symmetry between the projectile and the target atom in a binary collision, an example can be added of pronounced  $Z_1$  oscillations discovered experimentally in electronic energy loss of moderate-velocity ions transmitted through thin foils [40,41]. The elementary collision process here may be viewed as ion collision with an electron of the medium, the latter being pointlike, as in our present consideration, with a proviso that at collision velocity  $v$  below the Bohr velocity the atomic electrons cannot be regarded as free.

About as large  $Z_1$  oscillations were observed [42] in backscattering (as opposed to small-angle scattering considered in the present paper) of very low-energy ions, when the loss is predominantly nuclear, i.e., is due to elastic scattering

of atoms as a whole. Even greater  $Z_1$  oscillations were found in grazing reflection of ions from a crystal surface [43] and in channeling of ions transmitted through a crystal [44,45], in the latter case being important for ion implantation [46]. In all those  $Z_1$  oscillations the  $Z_1^{1/3}$  periodicity was not reported; they look less regular, although in general the minima and maxima match with those in our Fig. 8. The  $Z^{1/3}$ -periodic dependences are thus generally not so unusual in atomic physics, but their manifestation is process dependent and seems to be enhanced in scattering with certain momentum transfers or in channeling, due to certain restrictions on the particle motion. From the modern perspective, additional control of the particle dynamics is possible with the aid of bent crystals, in which the bending radius is a tunable parameter (see, e.g., [47–50] and references therein).

#### IV. WEAK SCREENING OF RUTHERFORD ASYMPTOTICS

Deviations from the TF approximation must arise as well for large momentum transfers but be related there mostly to inner shells, because large  $q$  correspond to small  $r$ . Clearly, inner shells are not amenable to the TF treatment. Instead, they are hydrogenic, which also promises simplicity.

In the extreme high- $q$  limit,  $d\sigma/d\sigma_R \xrightarrow{q \rightarrow \infty} 1$ , becoming completely independent of the electron distribution. However, as Figs. 5–7 indicate, unity is approached rather slowly, seemingly by a power law (weak screening [7–9]). The characteristic number in this case should be the coefficient in the subleading asymptotics. Its  $Z$  dependence may now be explored for shell effects. However, different existing theories predict different values even for the index of the power law in the subleading asymptotics, as will be delineated here shortly.

Many investigations of atomic scattering were based on the TF approximation for electron densities. It predicts a  $d\sigma^{\text{TF}}/d\sigma_R - 1 \sim q^{-3/2}$  asymptotic law, as evaluated in Appendix B for arbitrary  $\alpha$  in the eikonal approximation:

$$\frac{d\sigma^{\text{TF}}}{d\sigma_R} \underset{q \rightarrow \infty}{\simeq} 1 - \sqrt{2\pi} \left( \frac{\hbar}{qa_{\text{TF}}} \right)^{3/2} C_{\text{TF}}(\alpha). \quad (65)$$

The coefficient  $C_{\text{TF}}(\alpha) > 0$ , inferred from Eq. (B9), looks somewhat complicated,

$$C_{\text{TF}}(\alpha) = -\frac{7}{3} \text{Re} \frac{\text{B}\left(1 - i\alpha, \frac{7}{4} + i\alpha\right)}{\text{B}\left(1 + i\alpha, -\frac{3}{4} - i\alpha\right)}, \quad (66)$$

but is simplified in limiting cases.

In the large- $\alpha$  (semiclassical) limit (in fact, already at  $\alpha > 1$ ) it scales as<sup>3</sup>

$$C_{\text{TF}}(\alpha) \underset{\alpha \gg 1}{\simeq} \frac{7\Gamma(\frac{1}{4})}{3\Gamma(\frac{3}{4})} \alpha^{3/2} = 6.90 \alpha^{3/2}. \quad (67)$$

<sup>3</sup>Straightforward derivation of (67) from (66) is lengthy, because at large  $\alpha$  the real part of the Beta function ratio in (66) is subdominant to its imaginary part. The derivation will be skipped herein, but this relationship can be easily checked numerically with any desired accuracy.

This corresponds to the asymptotics of the classical differential cross section [see Appendix B 1, Eq. (B5)]:

$$\frac{d\sigma_{\text{cl}}^{\text{TF}}}{d\sigma_R} \underset{Q \rightarrow \infty}{\simeq} 1 - \frac{7\text{B}\left(\frac{1}{2}, \frac{1}{4}\right)}{6(a_{\text{TF}}Q)^{3/2}}.$$

In the opposite limit  $\alpha \rightarrow 0$  the coefficient turns to unity,

$$C_{\text{TF}}(0) = -\frac{7}{3} \frac{\Gamma(\frac{7}{4})}{\Gamma(1 + \frac{7}{4})} \frac{\Gamma(1 - \frac{3}{4})}{\Gamma(-\frac{3}{4})} = 1,$$

and the cross section ratio becomes

$$\frac{d\sigma^{\text{TF}}}{d\sigma_R} \underset{Q \rightarrow \infty}{\simeq} 1 - \sqrt{2\pi} \left( \frac{\hbar}{qa_{\text{TF}}} \right)^{3/2}. \quad (68)$$

However, it appears to differ from the asymptotics of the Born expansion for a generic  $n_e(r)$ , obtained from Eq. (51):

$$\begin{aligned} \frac{d\sigma_1}{d\sigma_R} \underset{Q \rightarrow \infty}{\simeq} & \left[ 1 + \frac{\pi}{2Z} n'_e(0) \left( \frac{2\hbar}{q} \right)^4 \right]^2 \\ & = 1 - \frac{2\pi}{a_{\text{B}}} n_e(0) \left( \frac{2\hbar}{q} \right)^4. \end{aligned} \quad (69)$$

[In the second equality, Kato's theorem (10) was employed.] The power law (69) has index 4, which is greater than that in (68). In the TF approximation though,  $n_e(0)$  would be infinite, so these approximations are just mutually incompatible.

The problem of the power correction to the Rutherford asymptotics was also addressed in the pioneering work by Molière [28], who treated the scattering problem in the eikonal approximation and obtained a structure

$$\frac{d\sigma_{\text{M}}}{d\sigma_R} \underset{q \rightarrow \infty}{\simeq} 1 - 2 \left( \frac{\mu_0}{Q} \right)^2 \ln \frac{Q}{\mu_1}, \quad (70)$$

with parameters  $\mu_0$  and  $\mu_1$  generally depending on the screening function and  $\alpha$ . Here the power-law index is equal to 2, being at variance with both (65) and (69). It is essential that (70) was based on Molière's parametrization [28] of the TF potential, which mitigates the TF electron density singularity in the origin, but rather deliberately, not in a way truly related to the atomic shell structure. This may have an effect on the subleading asymptotics.

#### A. Power correction to the Rutherford asymptotics

To get a reliable prediction for the weak-screening correction, we will calculate it here from scratch. That is easy to do now based on the representations established in Sec. II. Let us begin, again, with the classical case.

##### 1. Classical high- $Q$ subleading asymptotics

In Sec. II B 1 the leading-order Rutherford asymptotics of the classical scattering cross section was obtained by sending  $b \rightarrow 0$ . The correction to it follows by extending the expansion of the radicals in the integrands of (25a) and (32b) to the next order,

$$r\sqrt{r^2 - b^2} \underset{b \rightarrow 0}{\simeq} r^2 - \frac{b^2}{2}, \quad r^3/\sqrt{r^2 - b^2} \underset{b \rightarrow 0}{\simeq} r^2 + \frac{b^2}{2}, \quad (71)$$

and integrating termwise

$$S_1 \underset{b \rightarrow 0}{\simeq} 1 - \frac{b^2}{2} \langle r^{-2} \rangle, \quad (72)$$

$$S_2 \underset{b \rightarrow 0}{\simeq} 1 + \frac{b^2}{2} \langle r^{-2} \rangle \simeq \frac{1}{S_1} \quad (73)$$

(cf. the inset of Fig. 3). Here

$$\langle r^{-2} \rangle = \frac{4\pi}{Z} \int_0^\infty dr n_e(r) \quad (74)$$

is the expectation value [according to the definition (47)] of the inverse-square radius of an atomic electron.

In a more elucidating way, Eq. (72) can be derived from (24):

$$S_1(0) - S_1(b) = \frac{2\pi}{Z} \int_0^b db' b' \int_{-\infty}^\infty dz n_e(b', z) \quad (75a)$$

$$\underset{b \rightarrow 0}{\simeq} \frac{\pi}{Z} b^2 \int_{-\infty}^\infty dz n_e(0, z) = \frac{b^2}{2} \langle r^{-2} \rangle. \quad (75b)$$

The integration in (75a) runs over a cylinder of radius  $b$ , whose axis is parallel to the fast particle velocity and passes through the atom nucleus. The exterior of this charged [with density  $n_e(r)$ ] cylinder does not exert a force on the particle inside it, whereas the cylinder interior constitutes the difference from the pointlike nucleus charge. As  $b \rightarrow 0$ , the cylinder shrinks to a charged string (75b), the integration along which yields  $\langle r^{-2} \rangle$ .

Introducing (72) and (73) in (31), we obtain the weak-screening correction to the differential cross-section ratio

$$\frac{d\sigma_{cl}}{d\sigma_R} \underset{Q \rightarrow \infty}{\simeq} 1 - \frac{2}{Q^2} \langle r^{-2} \rangle. \quad (76)$$

It has the same  $Q$  index equal to 2 as Molière's Eq. (70), but does not contain a logarithm of  $Q$ .

The absence of the logarithm can now be readily understood. As we noted above, Molière's calculation, unlike ours, employs his parametrization for the atomic potential. With the aid of (5), one can express (74) through the atomic potential as

$$\int_0^\infty dr n_e(r) \propto \int_0^\infty \frac{dr}{r} g''(r). \quad (77)$$

If  $g(r)$  were parametrized here so that its connection with  $n_e(r)$  via the condition (6) were abolished, the integral (77) generally would logarithmically diverge at small  $r$ . As is shown in Appendix C, the physical regularization of this divergent integral is effectively provided by the impact parameter, which is reciprocal to  $q$  and so gives rise to  $\ln q$ .

If instead of Molière's parametrization the Thomas-Fermi model  $g(r) = \phi_{TF}''(\xi)$  were employed, the integral in Eq. (77) would diverge at small  $r$  by a power law [cf. Eq. (B1)] and this would yield a greater power of  $q$ . That is chained to the fact that for the Thomas-Fermi screening function the condition (8) is violated severely:  $\phi_{TF}''(0) = \infty$ .

The accuracy of the asymptotics (76) for silicon as an example is shown in Fig. 12. The asymptotic approximation holds well for  $a_{TF}Q \gtrsim 15$ . This is congruent with  $b/a_{TF} \lesssim 15$  in the parabolic region of  $S_1(b)$  and  $S_2(b)$  in the inset of Fig. 3.

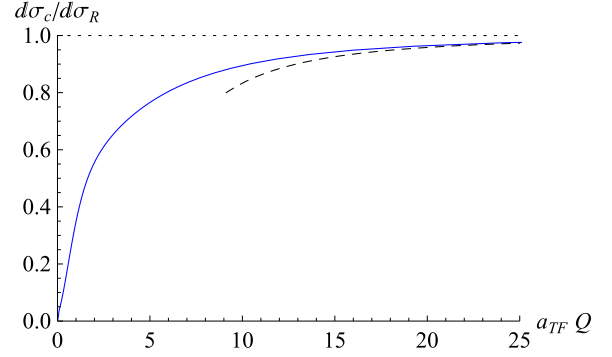


FIG. 12. The solid curve shows the ratio of the differential cross section of high-energy classical scattering on a silicon atom ( $Z = 14$ ) to the Rutherford cross section. The electron charge density in Eqs. (31), (25a), and (32b) is evaluated by the HF parametrization [20]. The dashed curve shows asymptotics (76), with  $\langle r^{-2} \rangle$  taken from HF tables [56]. For comparison with TF approximation, see Fig. 5.

As for the TF approximation, it is evident from Fig. 5 that at such high  $Q$  it is far from being accurate.

## 2. Eikonal calculation

In the quantum case, one needs at first to find the sub-leading small- $b$  expansion for the eikonal phase. To this end, it suffices to integrate expansion (72) for  $S_1(b)$  according to Eqs. (43) and (45):

$$S_0(b) \underset{b \rightarrow 0}{\simeq} \ln \frac{b}{b_0} - \frac{\langle r^{-2} \rangle}{4} b^2. \quad (78)$$

Correspondingly, the regular part of the phase factor expands as

$$e^{2i\alpha S_0} \underset{b \rightarrow 0}{\simeq} \left( \frac{b}{b_0} \right)^{2i\alpha} \left( 1 - 2i\alpha \frac{\langle r^{-2} \rangle}{4} b^2 \right).$$

On inserting this into Eq. (50) and integrating over  $b$  or  $\xi$  with the aid of the formula

$$\int_0^\infty d\xi \xi^{1+2(n+i\alpha)} J_0(\xi) = 2^{1+2(n+i\alpha)} \frac{\Gamma(1+n+i\alpha)}{\Gamma(-n-i\alpha)}, \quad (79)$$

we are led to

$$\begin{aligned} \frac{d\sigma}{d\sigma_R} \underset{Q \rightarrow \infty}{\simeq} & \left| 1 + \frac{2i\alpha(1+i\alpha)^2}{(2\alpha Q)^2} \langle r^{-2} \rangle \right|^2 \\ & \simeq 1 - \frac{2}{Q^2} \langle r^{-2} \rangle. \end{aligned} \quad (80)$$

Remarkably, this coincides with the classical result (76), by virtue of the fact that in the squared amplitude the dependence on  $\alpha$ , and therewith on  $\hbar$ , has canceled in the given order.

Since Eq. (80) is fully quantal, it can be compared with the first Born approximation (69). Equation (80) predicts a lower falloff index, thus giving a more dominant contribution. However, there is no actual contradiction with (69), insofar as (80) with  $Q^{-2} = (2\hbar\alpha/q)^2$  corresponds to a *higher order* in  $\alpha$ .

## B. The $Z$ dependence of $\langle r^{-2} \rangle$

Having pinned down the index of the asymptotic law, we are now ready to explore shell effects in its coefficient (74). That can be done, again, by computing its  $Z$  dependence.

### 1. Nonrelativistic $K$ shell

As was pointed out in Sec. IV A 1, in the TF approximation  $\langle r^{-2} \rangle$  diverges at small  $r$ , because  $n_e(r)$  blows up at  $r \rightarrow 0$  strongly. In a HF treatment, there will be no divergence, but it is plausible that  $\langle r^{-2} \rangle$  will be dominated by inner shells. From Fig. 2(a) (pertaining to silicon, but being typical for all the elements) it is evident that the integral (74) must primarily be dominated by the  $K$  shell. If the two electrons in this shell are described by purely hydrogenic nonrelativistic wave functions,

$$n_e(r) = n_K(r) = \frac{2}{\pi} \left( \frac{Z}{a_B} \right)^3 e^{-2Zr/a_B}, \quad (81)$$

their aggregate contribution to  $\langle r^{-2} \rangle$  amounts to

$$\langle r^{-2} \rangle_K = 4(Z/a_B)^2. \quad (82)$$

However, contributions from the other shells should not be just omitted.

### 2. Higher shells

To approximately account for higher-shell contributions, begin with quoting the generic formula for the expectation value  $\langle r^{-2} \rangle$  for an arbitrary single-electron nonrelativistic hydrogenic bound state [2,51]:

$$\langle r^{-2} \rangle_{nl}^{\text{nonrel}} = \frac{(Z/a_B)^2}{n^3(l + \frac{1}{2})}. \quad (83)$$

This sufficiently simple form can be summed over all spin states, angular momentum numbers  $m$  and  $l$ , and all principal quantum numbers  $n$  up to infinity, if we assume that high shells, even though not hydrogenic, do not contribute significantly:

$$\begin{aligned} Z \langle r^{-2} \rangle \underset{Z \rightarrow \infty}{\simeq} 2 \sum_{nlm} \langle r^{-2} \rangle_{nl} &= 2 \sum_{n=1}^{\infty} \frac{(Z/a_B)^2}{n^3} \sum_{l=0}^{n-1} \sum_{m=-l}^l \frac{1}{l + \frac{1}{2}} \\ &= 4 \left( \frac{Z}{a_B} \right)^2 \sum_{n=1}^{\infty} n^{-2} = \frac{2\pi^2}{3} \left( \frac{Z}{a_B} \right)^2. \end{aligned} \quad (84)$$

The latter result must be thought of as the large- $Z$  scaling law for  $\langle r^{-2} \rangle$  of a nonrelativistic atom.

However, the sum  $\sum n^{-2}$  with the increase of  $n$  actually converges too slowly and for finite  $Z$  stays considerably below the limiting value (84). On the other hand, the residual difference depends on  $Z$  smoothly. A simple TF-based power-law formula for it was given in [52]:

$$\frac{a_B^2}{4Z} \langle r^{-2} \rangle_{\text{DP}} \underset{Z \rightarrow \infty}{\simeq} \frac{\pi^2}{6} - 1.508Z^{-1/3}. \quad (85)$$

With the increase of  $Z$ , the approximation (85) improves and approaches the predictions of nonrelativistic HF calculations [53] (see the red dashed curve in Fig. 13).

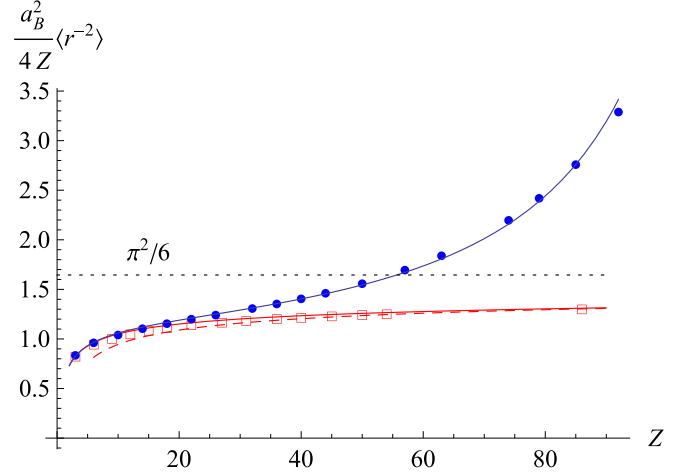


FIG. 13. Atomic mean inverse square radius (74) in units of its nonrelativistic  $K$ -shell contribution evaluated by Eq. (82). Open squares show calculations of [54,55] based on nonrelativistic HF distributions [53]. The red dashed curve shows the nonrelativistic interpolation formula (85) taking into account higher shells. The red solid curve shows the fit (86) to the nonrelativistic HF data. Closed blue circles show the calculation based on relativistic HF tables [56]. The blue solid curve shows Eq. (97), taking into account relativistic corrections for  $K$ ,  $L_I$ , and  $L_{II}$  shells.

An even better approximation can be achieved if both the coefficient and the index of the power correction are treated as fitting parameters. The fit

$$\frac{a_B^2}{4Z} \langle r^{-2} \rangle_{\text{fit}}^{\text{nonrel}} \approx \frac{\pi^2}{6} - 1.1Z^{-0.267} \quad (86)$$

is accurate enough for virtually all  $Z$  (see the red solid curve in Fig. 13). It proves to hold even for  $Z \leq 7$ , when the right-hand side of (86) already subsides below the pure hydrogenic  $K$ -shell contribution (82). This reflects the fact that at low  $Z$  the electron wave functions cease to be perfectly hydrogenic: The repulsion between electrons becomes comparable to their attraction to the nucleus even for the lowest shells. That increases typical  $r$  and in turn decreases  $\langle r^{-2} \rangle$ .

### 3. Relativistic effects

Physically, however, it should be noted that the limit (84) is not approached at  $Z \rightarrow \infty$  at all, because inner shells in this limit become relativistic. Since at high  $Z$  those shells are hydrogenic, they can be described fully relativistically by solving the Dirac equation.

The counterpart of the formula (83) for a Dirac electron in a Coulomb field has the form [57]

$$\langle r^{-2} \rangle_{nlj} = \frac{2(Z/a_B)^2 (1 - \varepsilon_{nlj}^2)^{3/2} \kappa (2\kappa \varepsilon_{nlj} - 1)}{\zeta^3 \sqrt{\kappa^2 - \zeta^2} [4(\kappa^2 - \zeta^2) - 1]}. \quad (87)$$

Here

$$\varepsilon_{nlj} = \left( 1 + \frac{\zeta^2}{(n_r + \sqrt{\kappa^2 - \zeta^2})^2} \right)^{-1/2}, \quad \zeta = \frac{Ze^2}{\hbar c} \quad (88)$$

is the bound electron energy in units of  $mc^2$ , in a state with the principal quantum number  $n = n_r + |\kappa| = 1, 2, 3, \dots$ , orbital angular momentum  $l$ , and total angular momentum  $j = l \pm \frac{1}{2}$ . The parameter  $\kappa$  is conventionally defined as

$$\kappa = -(j + \frac{1}{2}) \text{sgn}(\mathbf{l} \cdot \mathbf{s}) = \begin{cases} l & \text{if } j = l - \frac{1}{2} \\ -(l + 1) & \text{if } j = l + \frac{1}{2}. \end{cases} \quad (89)$$

In the nonrelativistic limit  $\zeta \rightarrow 0$ , Eq. (87) reduces to

$$\langle r^{-2} \rangle_{nlj} \underset{Ze^2 \rightarrow 0}{\approx} \frac{2(Z/a_B)^2}{(n_r + |\kappa|)^3 (2|\kappa| + \text{sgn} \kappa)}, \quad (90)$$

and since  $2|\kappa| + \text{sgn} \kappa = 2l + 1$  for both  $\kappa = l$  and  $\kappa = -(l + 1)$ , the nonrelativistic formula (83) is recovered.

Since, according to its definition (89),  $|\kappa|$  is an integer greater than zero, the right-hand side of (87) as a function of  $Z$  has singularities at

$$\frac{Ze^2}{\hbar c} = \sqrt{1 - \frac{1}{4}}, 1, \sqrt{2^2 - \frac{1}{4}}, 2, \sqrt{3^2 - \frac{1}{4}}, 3, \dots$$

The first singularity is encountered when the factor  $4(\kappa^2 - \zeta^2) - 1$  in the denominator of (87) turns to zero for  $|\kappa| = 1$ , i.e., at

$$Z = \frac{\sqrt{3}\hbar c}{2e^2} = 118.7. \quad (91)$$

This is the same value at which the conditions (7) and (8) break down. As yet, no elements have been discovered with  $Z > 118$ .

We now apply formula (87) to the lowest shells, which must be the most relativistic. Each of the two electrons in the  $K$  shell (the ground state  $1s_{1/2}$ ) has quantum numbers

$$\kappa = -1, \quad n_r = 0.$$

Therewith (88) simplifies to

$$\varepsilon_{1s_{1/2}} = \sqrt{1 - \zeta^2}$$

and Eq. (87) yields

$$\langle r^{-2} \rangle_{1s_{1/2}} = 2 \left( \frac{Z}{a_B} \right)^2 \frac{1}{\sqrt{1 - \zeta^2} (2\sqrt{1 - \zeta^2} - 1)}. \quad (92)$$

The  $Z$  dependence of the last, relativistic factor in (92) is illustrated in Fig. 14 by the solid curve. For example, for lead ( $Z = 82$ ) it exceeds 2.

Each of the two electrons in the  $L_I$  shell ( $2s_{1/2}$  state) has quantum numbers

$$\kappa = -1, \quad n_r = 1.$$

Insertion thereof to Eq. (88) gives the term energy

$$\varepsilon_{2s_{1/2}} = \sqrt{\frac{1 + \sqrt{1 - \zeta^2}}{2}},$$

while (87) is written as

$$\langle r^{-2} \rangle_{2s_{1/2}} = \frac{1}{8} \langle r^{-2} \rangle_{1s_{1/2}} N_{2s_{1/2}}(\zeta), \quad (93)$$

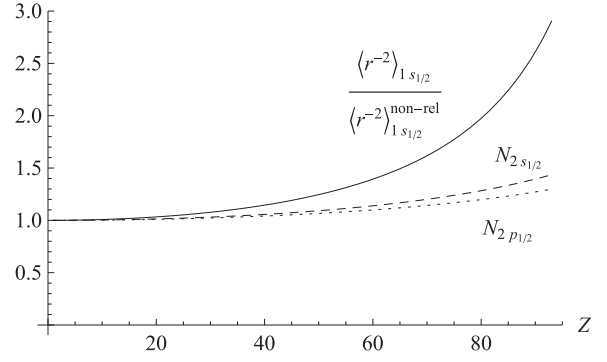


FIG. 14. The  $Z$  dependence of relativistic factors characterizing  $K$ ,  $L_I$ , and  $L_{II}$  shells. The solid curve shows  $\langle r^{-2} \rangle_{1s_{1/2}}$  for the  $K$  shell, evaluated by Eq. (92), relative to its nonrelativistic counterpart  $\langle r^{-2} \rangle_{1s_{1/2}}^{\text{non-rel}} = 2Z^2/a_B^2$ . The dashed curve shows the additional factor  $N_{2s_{1/2}}(Ze^2/\hbar c)$  for the  $L_I$  shell, evaluated by Eq. (94). The dotted curve shows the factor  $N_{2p_{1/2}}(Ze^2/\hbar c)$  for the  $L_{II}$  shell, evaluated by Eq. (96).

with

$$N_{2s_{1/2}}(\zeta) = \frac{2}{(1 + \sqrt{1 - \zeta^2})^{3/2} (\sqrt{1 + \sqrt{1 - \zeta^2}} - 2^{-1/2})}. \quad (94)$$

Both factors  $\langle r^{-2} \rangle_{1s_{1/2}}$  and  $N_{2s_{1/2}}$  in (93) include relativistic effects, but as Fig. 14 shows, the  $Z$  dependence of  $N_{2s_{1/2}}$  is weaker. This is because  $\langle r^{-2} \rangle_{1s_{1/2}}$  given by Eq. (92) contains in the denominator two factors vanishing at  $\zeta = \sqrt{3}/2$  and  $\zeta = 1$ , whereas  $N_{2s_{1/2}}$  is finite for  $\zeta \leq 1$ .

Similarly, each electron in the  $L_{II}$  shell ( $2p_{1/2}$  state) is characterized by

$$\kappa = 1, \quad n_r = 1, \quad \varepsilon_{2p_{1/2}} = \varepsilon_{2s_{1/2}}$$

and Eq. (87) gives

$$\langle r^{-2} \rangle_{2p_{1/2}} = \frac{1}{24} \langle r^{-2} \rangle_{1s_{1/2}} N_{2p_{1/2}}(\zeta), \quad (95)$$

with

$$N_{2p_{1/2}}(\zeta) = \frac{6}{(1 + \sqrt{1 - \zeta^2})^{3/2} (\sqrt{1 + \sqrt{1 - \zeta^2}} + 2^{-1/2})}. \quad (96)$$

The  $\zeta$  dependence of  $N_{2p_{1/2}}$  (dotted curve in Fig. 14) is slightly weaker than for  $N_{2s_{1/2}}$ .

For  $2p_{3/2}$  and higher shells, relativistic effects are negligible [58]. The relativistic effects for the aggregate  $\langle r^{-2} \rangle$  can thus be taken into account by summing the corresponding corrections for the  $K$  (two electrons),  $L_I$  (two electrons), and  $L_{II}$  (two electrons) shells. Given that the relative contributions of the  $L_I$  and  $L_{II}$  shells are not large, it is admissible to approximate the  $N_{2s_{1/2}}$  and  $N_{2p_{1/2}}$  factors by  $N_{2s_{1/2}}(0) = N_{2p_{1/2}}(0) = 1$ . Therewith, in the sum of relativistic contributions, the relatively simple structure (92) factors out:

$$\begin{aligned} & 2\langle r^{-2} \rangle_{1s_{1/2}} + 2\langle r^{-2} \rangle_{2s_{1/2}} + 2\langle r^{-2} \rangle_{2p_{1/2}} \\ & \approx 2\left(1 + \frac{1}{8} + \frac{1}{24}\right) \langle r^{-2} \rangle_{1s_{1/2}} = \frac{7}{3} \langle r^{-2} \rangle_{1s_{1/2}}. \end{aligned}$$

Subtracting the corresponding nonrelativistic contribution and adding to the full nonrelativistic result (86), we get

$$\frac{q_B^2}{4Z} \langle r^{-2} \rangle \approx \frac{\pi^2}{6} - 1.1Z^{-0.267} + \frac{7}{6} \left( \frac{1}{\sqrt{1-\zeta^2}(2\sqrt{1-\zeta^2}-1)} - 1 \right). \quad (97)$$

This combined approximation proves to be sufficiently close to the relativistic HF calculations [56] (see the blue curve in Fig. 13).

We conclude that the  $Z$  dependence of  $\langle r^{-2} \rangle$  is monotonic, but nonuniform (see Fig. 13), in spite of the dominance of inner shells. With the increase of  $Z$  from its lowest values, the increase of  $\langle r^{-2} \rangle/Z$  due to the accumulation of higher shells gradually slows down, but at  $Z > 40$  the inner-shell contributions get enhanced by relativistic effects, owing to which the dependence of  $\langle r^{-2} \rangle/Z$  on  $Z$  accelerates again.

### V. SHELL CORRECTIONS TO THE MOLIÈRE SCREENING ANGLE

Hitherto we analyzed the differential cross section of single atomic scattering. To observe it directly in an experiment requires a particularly thin target, no thicker than a few nanometers for a solid. For more practical and less fragile targets, such a condition is not met, and the scattering is multiple. What is observed then is the particle angular distribution function, which is to be found from the solution of a linear transport equation.

Conventionally, this problem is treated in terms of deflection angles, which are related to the momentum transfers we dealt with above simply by

$$\chi = q/p, \quad (98)$$

where  $p$  is the large longitudinal momentum, assumed to be nearly conserved in the course of the particle passage through-out the target. It follows that the single-scattering angle (98), as well as the aggregated deflection angle  $\theta$ , is small compared to a radian, so in the transport equation they may be approximated by transverse vectors:

$$\frac{\partial f}{\partial l} = n_a \int d\sigma(\chi) [f(\theta - \chi, l) - f(\theta, l)]. \quad (99)$$

Here  $f(\theta, l) = f(\theta, l)$  is the particle distribution function at the traversed length  $l$ ,  $d\sigma(\chi) = d^2\chi \frac{d\sigma}{d^2\chi}$  is the differential cross section of particle scattering on a single atom through angle  $\chi$ , and  $n_a$  is the density of atoms in the medium.

The solution of the transport equation (99) with initial condition  $f(\mathbf{0}, l) = \delta(\theta)$  is obtained as a Fourier-Bessel integral with the integrand depending on the target thickness purely exponentially:

$$f(\theta, l) = \frac{1}{2\pi} \int_0^\infty d\rho \rho J_0(\rho\theta) \times \exp\left(-n_a l \int d\sigma(\chi) [1 - J_0(\rho\chi)]\right). \quad (100)$$

Now when  $n_a\sigma l$  in the exponent is large, the target may be regarded as physically thick and the scattering process as

multiple. The sharply peaking exponential in the integrand of (100) may then be replaced by its small- $\rho$  asymptotics. Taking into account the Coulomb character of atomic scattering, the exponent needs to be evaluated with the next-to-leading logarithmic accuracy, which leads to Molière's theory [26,59,60]. The corresponding approximate solution reads<sup>4</sup>

$$f(\theta, l) = \frac{1}{2\pi} \int_0^\infty d\rho \rho J_0(\rho\theta) \exp\left(-\frac{\chi_c^2 \rho^2}{2} \ln \frac{2}{\chi'_a \rho}\right). \quad (101)$$

Here

$$\chi_c^2 = 4\pi n_a l \left(\frac{Z_1 Z e^2}{pv}\right)^2 \quad (102)$$

encapsulates the target thickness and density, whereas all the atomic characteristics in this thick-target (angular diffusion) limit enter the Molière screening angle [59,60]

$$\chi'_a = q'_a/p. \quad (103)$$

The energy-independent number  $q'_a$  characterizing the target atoms is defined by

$$\ln q'_a(\alpha) = \lim_{q_R \rightarrow \infty} \left( \ln q_R - \int_0^{q_R} \frac{dq}{q} \frac{d\sigma}{d\sigma_R} \right) + \gamma_E - 1, \quad (104)$$

with  $\gamma_E = 0.577$  Euler's constant. The inverse of  $q'_a$  may be thought of as an analog of the screening radius.<sup>5</sup>

With  $d\sigma/d\sigma_R$  generally depending on both  $Z$  and  $\alpha$ , so does  $q'_a$ . However, the  $\alpha$  dependence of  $q'_a$ , known as the Coulomb correction, appears to entirely factor out from the  $Z$  dependence (see, e.g., [62] and references therein). For characterization of the  $Z$  dependence alone, it is thus sufficient to investigate the Born limit  $q_a(0)$ . That will be our task in the present section.

Inserting  $d\sigma/d\sigma_R$  from Eq. (51) into Eq. (104) and performing the  $q$  integration prior to  $r$  and  $r'$  integrations with the aid of the formula

$$\lim_{q_R \rightarrow \infty} \left[ \ln \frac{q_R}{\hbar} - \int_0^{q_R} \frac{dq}{q} \left(1 - \frac{\sin qr/\hbar}{qr/\hbar}\right) \left(1 - \frac{\sin qr'/\hbar}{qr'/\hbar}\right) \right] + \gamma_E - 1 = W(r, r'), \quad (105)$$

where

$$W(r, r') = \ln \frac{r+r'}{rr'} + \frac{(r-r')^2}{4rr'} \ln \frac{r+r'}{|r-r'|} - \frac{1}{2}, \quad (106)$$

<sup>4</sup>The neglect of the size of atomic nuclei in Eq. (101) implies that the typical accumulated momentum transfers  $p\theta \propto (n_a l)^{1/2}$  are still small at the nuclear scale, i.e., the target thickness is not too large, which is usually fulfilled in practice. Even if the nuclear size is taken into account [26,61], the theory involves the parameters (103) and (104), which will be our object of study herein.

<sup>5</sup>The prime in  $q'_a$  (not to be confused with a derivative) is a convention to distinguish it from  $q_a = e^{1/2-\gamma_E} q'_a = 0.926q'_a$  [60]. The limit  $q_R \rightarrow \infty$  in (104) physically implies that  $q_R \gg q'_a$ . It may also be worth noting that, if in (104) on the upper limit it were possible to set  $q_R = \infty$ , this integral would be proportional to the mean-square momentum transfer.

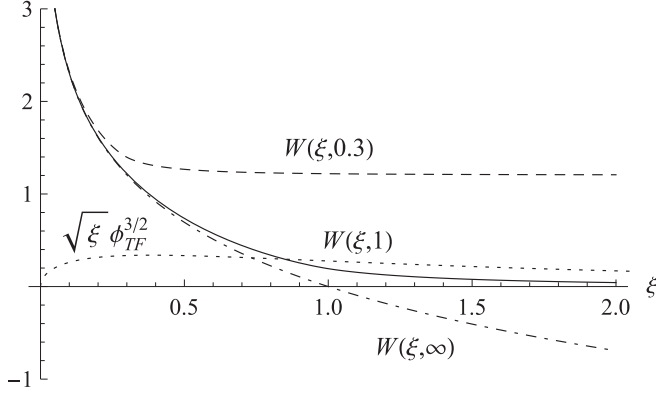


FIG. 15. Function  $W(\xi, \xi') = W(\xi', \xi)$ , the kernel in the integral expression (107) of the screening momentum logarithm through the atomic electron density. The solid curve shows  $W(\xi, 1) = W(1, \xi)$ , from which  $W(\xi, \xi')$  at any arguments  $\xi$  and  $\xi'$  can be reconstructed via relation (109), by a dilation in  $\xi$  and the addition of a constant. The dashed curve shows  $W(\xi, 0.3)$  and the dot-dashed curve  $W(\xi, \infty)$ . For comparison of spatial scales, the dotted curve shows also  $\sqrt{\xi}\phi_{\text{TF}}^{3/2}(\xi)$ , which multiplies  $W$  in Eq. (111).

we are led to a double-integral representation for the logarithm of Molière's screening momentum:

$$\ln \frac{q'_a(0)}{\hbar} = \frac{1}{Z^2} \int d^3r d^3r' n_e(r) n_e(r') W(r, r') \quad (107a)$$

$$= \left(\frac{4\pi}{Z}\right)^2 \int_0^\infty dr r^2 n_e(r) \int_0^\infty dr' r'^2 n_e(r') W(r, r') \quad (107b)$$

$$\equiv \langle W(r, r') \rangle. \quad (107c)$$

By partial integration in (107b) with the use of Eq. (5) it may be transformed to a somewhat simpler form in terms of the screening function,

$$\ln \frac{q'_a(0)}{\hbar} = \int_0^\infty dr g'(r) \int_0^r dr' g'(r') [\ln(r'^{-2} - r^{-2}) - 2], \quad (108)$$

but here we will stick to the representation (107b) involving the electron density.

The weighting function (106) diverges logarithmically at both small and large  $r$  and  $r'$ , reflecting the Coulomb character of the scattering. It has a scaling property

$$W(Cr, Cr') = -\ln C + W(r, r') \quad (109)$$

and so can be decomposed into a sum of two functions of single variables, e.g., by choosing  $C = 1/r'$ :

$$W(r, r') = -\ln r' + W(r/r', 1), \quad W(\infty, 1) = 0. \quad (110)$$

The behavior of  $W(r, r')$  for several fixed values of its second argument is shown in Fig. 15.

In the pure Thomas-Fermi model (18), employing Eq. (109) with  $C = a_{\text{TF}}^{-1}$  and  $a_{\text{TF}}(Z)$  defined by Eq. (14), we would get

$$\begin{aligned} \ln \frac{q'_a(0)a_{\text{TF}}}{\hbar} &= \int_0^\infty d\xi \sqrt{\xi} \phi_{\text{TF}}^{3/2}(\xi) \int_0^\infty d\xi' \sqrt{\xi'} \phi_{\text{TF}}^{3/2}(\xi') W(\xi, \xi') \\ &= 0.18. \end{aligned} \quad (111)$$

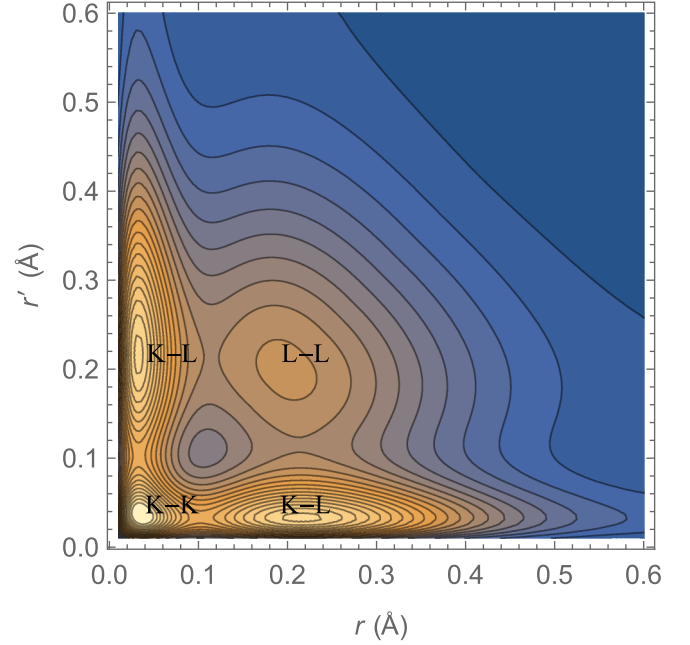


FIG. 16. Integrand of the integral (107b), determining the Molière screening momentum for a silicon atom. The  $K$ -shell and  $L$ -shell contributions and their interference are manifest as enhancements (bright spots). Electron densities for silicon, entering here as  $r$ - and  $r'$ -dependent factors, are given in Fig. 2.

This is somewhat higher than the value

$$\ln \frac{q'_a(0)a_{\text{TF}}}{\hbar} = \ln \sqrt{1.13} + \gamma_E - \frac{1}{2} = 0.14 \quad (112)$$

obtained by Molière [59] based on his parametrization for the TF potential.

To visualize the behavior of the integrand of the double integral in (107b), it is shown in Fig. 16 for a silicon atom. It exhibits a significant  $K$ -shell contribution (the brightest spot at  $r, r' \sim 0.03$  Å) and a sizable interference between the  $K$  and  $L$  shells (two prolate spots at  $r \sim 0.03$  Å and  $r' \sim 0.2$  Å and at  $r' \sim 0.03$  Å and  $r \sim 0.2$  Å). In general, inner shells give greater contribution than outer ones, but the interference between inner and intermediate shells is also noticeable.

To isolate shell contributions from the TF one, the latter needs to be subtracted, because it is expected to yield the monotonic part of the  $Z$  dependence. To this end, rewrite Eq. (107c) by adding  $\ln a_{\text{TF}}(Z)$  to both of its sides:

$$\ln \frac{q'_a(0)a_{\text{TF}}}{\hbar} = \langle W(r/a_{\text{TF}}, r'/a_{\text{TF}}) \rangle = \langle W \rangle(Z). \quad (113)$$

The right-hand side here is to be computed based on a HF density parametrization. The result for HF parametrization [20] is plotted in Fig. 17. Let us now inspect the latter dependence.

At  $Z < 5$ , the HF result is observed to be appreciably higher than the TF one. This may be attributed to the fact that a relatively large contribution comes from the  $K$  shell, which yields a charge density higher than average. A similar expectation was quoted in the Introduction. It may be expected further that with the increase of  $Z$ , the relative contribution of the  $K$  shell diminishes, whereby the atom on the average

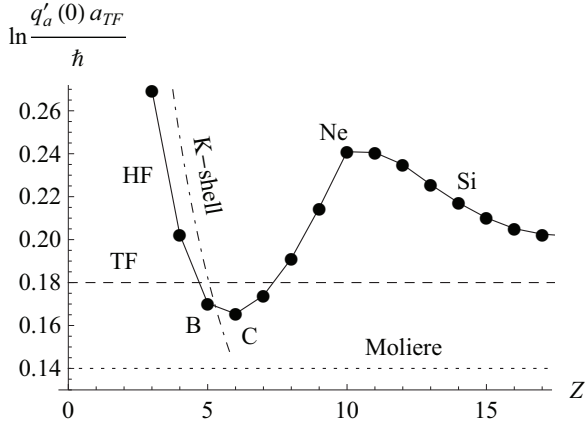


FIG. 17. The solid curve shows the  $Z$  dependence of  $\ln \frac{q'_a(0)a_{TF}}{\hbar}$  defined by Eqs. (113) and (106), with  $n_e$  parametrized by HF densities [20]. The dashed horizontal curve shows the TF result (111). The dot-dashed curve shows the  $K$ -shell contribution (114). For more details see the text.

swells. Indeed,  $\ln \frac{q'_a(0)a_{TF}}{\hbar}$  rapidly drops down in this region with the increase of  $Z$ .

The  $K$ -shell contribution to  $\ln \frac{q'_a(0)a_{TF}}{\hbar}$  can be isolated by replacing on the right-hand side of (113) the electron density with that of the (purely hydrogenic)  $K$  shell, given by Eq. (81):

$$\begin{aligned} \ln \frac{q'_a(0)a_{TF}}{\hbar} \Big|_K &= \left( \frac{4\pi}{Z} \right)^2 \int_0^\infty dr r^2 n_K(r) \\ &\quad \times \int_0^\infty dr' r'^2 n_K(r') W\left( \frac{r}{a_{TF}}, \frac{r'}{a_{TF}} \right) \\ &= \frac{1}{Z^2} \left( 4 \ln \frac{2Za_{TF}}{a_B} + \int_0^\infty d\xi \xi^2 e^{-\xi} \right. \\ &\quad \left. \times \int_0^\infty d\xi' \xi'^2 e^{-\xi'} W(\xi, \xi') \right) \\ &\equiv \frac{8}{3Z^2} (\ln Z + 0.1). \end{aligned} \quad (114)$$

The latter dependence, shown in Fig. 17 by the dot-dashed curve, is close to HF calculations up to  $Z = 5$ . (The agreement might be improved by taking into account the repulsion between the  $K$ -shell electrons.) Since this contribution falls off with  $Z$  rapidly enough, it does not require taking into account relativistic effects.

At  $Z = 5$  the decline halts, because an  $l = 1$  shell opens up [see Eq. (55)], allowing the atom to pack more compactly and contract relative to the TF approximation. (Note that this value of  $Z$  matches with a maximum in Fig. 8.) Correspondingly,  $\ln \frac{q'_a(0)a_{TF}}{\hbar}$  passes through a minimum and starts increasing again. The growth with respect to TF cannot continue indefinitely, and at  $Z = 10$  (neon) a maximum is achieved, corresponding to a minimum of the dependence in Fig. 8. Next, it turns down again, but the decrease is already slower. It is noteworthy that for most of the elements of the third period the value of  $q'_a$  is still greater than that for Be discussed in [5].

To summarize this section, shell effects for  $q'_a$  prove to be substantial too. The magnitude of the oscillations is

approximately 25%, which is commensurate with that for  $\frac{1}{a_{TF}Q} \frac{d\sigma_{cl}}{d\sigma_R} \Big|_{a_{TF}Q=0.3}$  exhibited in Fig. 8.

## VI. SUMMARY AND DISCUSSION

In this work it was established that despite the fact that shell effects in nonperturbative and multiple scattering are smeared out in angular distributions, they do persist in  $Z$  dependencies of certain characteristic determinants of the scattering differential cross section. A tentative explanation is that with a monotonic increase in  $Z$ , the allowed angular momenta of atomic orbitals increase in a stepwise manner. This causes the atom to alternately contract and swell with respect to its TF approximation, at the  $a_{TF}$  scale relevant here, inducing breather-type oscillations of various scattering observables. In any case, the  $Z$  dependence of the phase of those slowing oscillations is related not with that of Mendeleev's Periodic Table, but rather with that of its left step or Janet's variation.

The second, nonoscillatory type of shell effects is due to inner atomic shells, which cause a noticeable deviation of the differential cross section from the Rutherford asymptotics at large momentum transfers. Inner-shell contributions are significantly enhanced at high  $Z$  by relativistic effects.

There are also scattering observables, in which the two mentioned types of shell effects combine, as in the Molière screening angle, characterizing multiple Coulomb scattering. Being defined as an integral over a wide range of  $q$ , that quantity picks up commensurable contributions from all the shells. Since inner shells are compact, they increase the screening angle when  $Z$  is low, whereas intermediate shells give rise to its breather oscillations at larger  $Z$ .

As regards the perspective of experimental verification of the predicted effects, a few remarks can be added. Although the sensitivity of multiple-scattering angular distributions to Molière's screening angle is moderate and measurements may well be carried out in a wide range of projectile energies and target thicknesses, thinner targets should be favorable for that purpose. The sensitivity to shell effects can be enhanced yet by comparing the scattering distributions on C and Ne-Al targets, for which the shell effects are predicted to have opposite signs.

For measurement of single scattering, where shell effects must be the most pronounced, the use of thin foils or gaseous targets is essential. Such measurements are alleviated at high  $q$ , where the weak-screening correction to the Rutherford asymptotics can show up. It is desirable to determine this correction with a sufficient accuracy, since the asymptotic law  $d\sigma/d\sigma_R - 1 \sim q^{-2}$  itself [Eq. (80)], along with the relationship of its coefficient to  $\langle r^{-2} \rangle$ , demands verification. This single-scattering correction also has to be discriminated from the subleading power-law contribution  $\frac{\chi_c^2}{\theta^2} \ln \frac{\theta^2}{\chi_c^2}$  in multiple Coulomb scattering [63], which has the opposite sign. The way to such measurements has already been paved by experiments [7–9] with MeV light ions.

Most difficult seem to be measurements of single scattering at moderate  $q$ . There they are complicated by a sizable

probability of rescattering, but in reward the shell effects in that case should be the largest. To maximize the sensitivity to them, it may be worth exploiting the fact that deviations of the slope of  $d\sigma_{\text{cl}}/d\sigma_{\text{R}}$  from its TF value at  $Q \sim 0.3 a_{\text{TF}}^{-1}$  have opposite sign for Be and Ne-Al, so it may be worth comparing scattering on those elements in the first place.

### ACKNOWLEDGMENT

The author acknowledges support from the University of Pittsburgh within the Universities for Ukraine program.

### APPENDIX A: DERIVATION OF THE KATO THEOREM

For the reader's convenience, we will present here a simple derivation of Kato's relation (10). For an electron orbital characterized by orbital angular momentum  $l = 0$  and principal quantum number  $n$  (energy  $E$ ), the radial Schrödinger equation in a screened Coulomb field (1) reads

$$r \frac{d^2}{dr^2} R_{n0} + 2 \frac{d}{dr} R_{n0} + \frac{2m}{\hbar^2} [Er + Ze^2 g(r)] R_{n0} = 0, \quad (\text{A1})$$

where  $R_{nl}$  is the radial component of the wave function:  $\psi_{nlm}(r, \theta, \phi) = R_{nl}(r) Y_{lm}(\theta, \phi)$ . As  $r \rightarrow 0$ , the second derivative and the energy terms in Eq. (A1) vanish, giving rise to a relationship between the wave-function derivative in the origin and the nucleus charge:

$$\left. \frac{dR_{n0}}{dr} \right|_{r=0} = -\frac{Ze^2 m}{\hbar^2} R_{n0}(0).$$

Multiplication of its sides by  $2R_{n0}(0)$  converts it to a relation in terms of the probability density:

$$\left. \frac{dR_{n0}^2}{dr} \right|_{r=0} = -\frac{2Ze^2 m}{\hbar^2} R_{n0}^2(0) \equiv -\frac{2Z}{a_{\text{B}}} R_{n0}^2(0). \quad (\text{A2})$$

For nonzero orbital momenta ( $l \geq 1$ ), the radial Schrödinger equation demands that  $R_{nl} \underset{r \rightarrow 0}{\sim} r^l$  [2], whereby  $R_{nl}^2 \underset{r \rightarrow 0}{\sim} r^{2l} \rightarrow 0$ ,  $\frac{d}{dr} R_{n0}^2 \underset{r \rightarrow 0}{\sim} r^{2l-1} \rightarrow 0$ , and (A2) is sustained as well for  $l \geq 1$  (trivially, with both of its sides equal to zero). Insofar as it holds for any  $n$  and  $l$ , multiplication of both sides of (A2) by  $Y_{nl}^2(\theta, \phi)$  and summation over all  $l$  and  $n$  leads to the relation (10).

### APPENDIX B: THOMAS-FERMI HARD-SCATTERING ASYMPTOTICS

Realizing that the TF approximation is not strictly applicable for evaluation of the weak-screening correction to the Rutherford asymptotics, we will nonetheless derive it here for the sake of comparison with the more rigorous Eq. (80).

The solution of the TF equation (16) with boundary conditions (17) by power series in  $\xi$  is well known [64,65]:

$$\phi_{\text{TF}}(\xi) \underset{\xi \rightarrow 0}{\simeq} 1 - 1.59\xi + \frac{4}{3}\xi^{3/2}. \quad (\text{B1})$$

The coefficient of the linear term here can only be determined numerically, by solving the differential equation with both boundary conditions (17), whereas the coefficient preceding  $\xi^{3/2}$  follows from the differential equation (16) and boundary condition  $\phi_{\text{TF}}(0) = 1$  alone.

### 1. Classical hard scattering on the TF potential

In the classical case, inserting (B1) into (19) and (20) and integrating termwise with the aid of the integral

$$-\int_{-\infty}^{\infty} dz \frac{\partial}{\partial b} \frac{1}{(b^2 + z^2)^{s/2}} = \text{B}\left(\frac{1}{2}, \frac{s+1}{2}\right) \frac{s}{b^s}, \quad s > -1, \quad (\text{B2})$$

where  $\text{B}(x, y) = \Gamma(x)\Gamma(y)/\Gamma(x+y)$  is the Euler beta function, we observe that the term  $-1.59\xi$  in (B1) does not contribute, because it corresponds to  $s = 0$  (or, in physical terms, to an additive constant in the potential). The rest evaluates to

$$\begin{aligned} Q(b) &= -\frac{1}{2Z_1 Z e^2} \int_{-\infty}^{\infty} dz \frac{\partial}{\partial b} V(z, b) \\ &\underset{b \rightarrow 0}{\simeq} -\frac{1}{2} \int_{-\infty}^{\infty} dz \frac{\partial}{\partial b} \frac{1}{\sqrt{z^2 + b^2}} \\ &\quad -\frac{2}{3} a_{\text{TF}}^{-3/2} \int_{-\infty}^{\infty} dz \frac{\partial}{\partial b} (z^2 + b^2)^{1/4} \\ &= \frac{1}{b} \left[ 1 - \frac{\text{B}(\frac{1}{2}, \frac{1}{4})}{3} \left( \frac{b}{a_{\text{TF}}} \right)^{3/2} \right]. \end{aligned} \quad (\text{B3})$$

Inverting this relationship within the same subleading accuracy, one finds

$$b^2(Q) \underset{Q \rightarrow \infty}{\simeq} \frac{1}{Q^2} \left[ 1 - \frac{2}{3} \frac{\text{B}(\frac{1}{2}, \frac{1}{4})}{(a_{\text{TF}} Q)^{3/2}} \right]. \quad (\text{B4})$$

Next, inserting (B4) into (30) and differentiating, we obtain the cross section

$$\frac{d\sigma_{\text{cl}}^{\text{TF}}}{d\sigma_{\text{R}}} = Q^4 \left| \frac{db^2}{dQ^2} \right| \underset{Q \rightarrow \infty}{\simeq} 1 - \frac{7}{6} \frac{\text{B}(\frac{1}{2}, \frac{1}{4})}{(a_{\text{TF}} Q)^{3/2}}, \quad (\text{B5})$$

with  $\frac{7}{6} \text{B}(\frac{1}{2}, \frac{1}{4}) \approx 6.12$ . Therefore, in the TF approximation the correction to the Rutherford asymptotics appears in the order  $Q^{-3/2}$ , with the index lower than in (76).

### 2. Quantum hard scattering on the TF potential

The asymptotics for the quantum-mechanical scattering cross-section ratio (50) can be derived similarly. To this end, first the subleading small- $b$  asymptotics of  $S_0(b)$  needs to be found. It is retrieved straightforwardly by plugging the result (B3) into (43). There the integration gives

$$\begin{aligned} S_0^{\text{TF}}(b) &\underset{b \rightarrow 0}{\simeq} \ln \frac{b}{b_0} - \frac{\text{B}(\frac{1}{2}, \frac{1}{4})}{3} a_{\text{TF}}^{-3/2} \int_0^b db b^{1/2} \\ &= \ln \frac{b}{b_0} - \frac{2\text{B}(\frac{1}{2}, \frac{1}{4})}{9} \left( \frac{b}{a_{\text{TF}}} \right)^{3/2}. \end{aligned} \quad (\text{B6})$$

The eikonal amplitude involves an exponential of this function. The subleading asymptotics of the exponential readily follows from Eq. (B6):

$$e^{2i\alpha S_0^{\text{TF}}(b)} \underset{b \rightarrow 0}{\simeq} \left( \frac{b}{b_0} \right)^{2i\alpha} \left[ 1 - 2i\alpha \frac{2\text{B}(\frac{1}{2}, \frac{1}{4})}{9} \left( \frac{b}{a_{\text{TF}}} \right)^{3/2} \right]. \quad (\text{B7})$$

The integrals arising after substitution of (B7) into the impact parameter representation (50) of the eikonal scattering ampli-

tude can be evaluated by the generic formula

$$\int_0^\infty d\xi \xi^{1+2(n+i\alpha)} J_0(\xi) = 2^{1+2(n+i\alpha)} \frac{\Gamma(1+n+i\alpha)}{\Gamma(-n-i\alpha)}. \quad (\text{B8})$$

The differential cross-section ratio (50) then equals

$$\begin{aligned} \frac{d\sigma^{\text{TF}}}{d\sigma_{\text{R}}} \underset{q \rightarrow \infty}{\simeq} & \left| \frac{i}{2\alpha} \int_0^\infty d\xi \xi^{1+2i\alpha} J_0(\xi) \right. \\ & \left. + \frac{2\text{B}\left(\frac{1}{2}, \frac{1}{4}\right)}{9} \left(\frac{\hbar}{qa_{\text{TF}}}\right)^{3/2} \int_0^\infty d\xi \xi^{1+3/2+2i\alpha} J_0(\xi) \right|^2. \end{aligned}$$

The first term here gives a pure phase factor. It is therefore convenient to factor it out; after squaring, it gives unity:

$$\begin{aligned} \frac{d\sigma^{\text{TF}}}{d\sigma_{\text{R}}} \underset{q \rightarrow \infty}{\simeq} & \left| 1 + \frac{4}{9} \left(\frac{2\hbar}{qa_{\text{TF}}}\right)^{3/2} \text{B}\left(\frac{1}{2}, \frac{1}{4}\right) \right. \\ & \left. \times \frac{\Gamma(1-i\alpha)\Gamma\left(\frac{7}{4}+i\alpha\right)}{\Gamma(1+i\alpha)\Gamma\left(-\frac{3}{4}-i\alpha\right)} \right|^2. \end{aligned}$$

The arising products of Gamma functions can further be combined into Beta functions by the identities

$$\Gamma(1-i\alpha)\Gamma\left(\frac{7}{4}+i\alpha\right) = \Gamma\left(\frac{11}{4}\right)\text{B}\left(1-i\alpha, \frac{7}{4}+i\alpha\right),$$

$$\Gamma(1+i\alpha)\Gamma\left(-\frac{3}{4}-i\alpha\right) = \Gamma\left(\frac{1}{4}\right)\text{B}\left(1+i\alpha, -\frac{3}{4}-i\alpha\right).$$

Then with the identity  $\text{B}\left(\frac{1}{2}, \frac{1}{4}\right)\Gamma\left(\frac{11}{4}\right)/\Gamma\left(\frac{1}{4}\right) = \frac{21}{16}\sqrt{\pi}$  we are led to (65) and (66):

$$\frac{d\sigma^{\text{TF}}}{d\sigma_{\text{R}}} \underset{q \rightarrow \infty}{\simeq} 1 + \frac{7}{3}\sqrt{2\pi} \left(\frac{\hbar}{qa_{\text{TF}}}\right)^{3/2} \text{Re} \frac{\text{B}\left(1-i\alpha, \frac{7}{4}+i\alpha\right)}{\text{B}\left(1+i\alpha, -\frac{3}{4}-i\alpha\right)}. \quad (\text{B9})$$

### APPENDIX C: WEAK-SCREENING CORRECTION TO THE RUTHERFORD ASYMPTOTICS FOR A GENERIC SCREENING FUNCTION

Here we will derive the power correction to the Rutherford asymptotics of high- $q$  scattering in a screened Coulomb field, not enforcing the condition (8). It will be shown that the result will then qualitatively differ from (76), involving a logarithmic contribution and acquiring the same structure as Molière's (70).

#### 1. Evaluation of $S_0$

In classical mechanics the reduced momentum transfer (27a) is expressed via the derivative

$$Q(b) = \frac{\partial}{\partial b} S_0(b) \quad (\text{C1})$$

of the reduced eikonal phase (43), which is expressed through the atomic potential as [cf. Eq. (20)]

$$S_0(b) = - \int_b^\infty \frac{dr}{\sqrt{r^2 - b^2}} g(r). \quad (\text{C2})$$

In quantum mechanics, the scattering amplitude is expressed in terms of (an integral of an exponential of) the same function

$S_0(b)$ . In any case, we first need to evaluate the asymptotic expansion of (C2) in the limit  $b \rightarrow 0$  (corresponding to  $q \rightarrow \infty$ ) up to terms of order  $b^2$ .

To this end, taking into account the behavior of the factor in the integrand  $\frac{1}{\sqrt{r^2 - b^2}} \underset{b \rightarrow 0}{\simeq} \frac{1}{r} + \frac{b^2}{2r^3}$ , where both terms are singular functions of  $r$ , rearrange (C2) as

$$\begin{aligned} -S_0(b) = & \int_b^\infty dr \left( \frac{1}{\sqrt{r^2 - b^2}} - \frac{1}{r} - \frac{b^2}{2r^3} \right) g(r) \\ & + \int_b^\infty \frac{dr}{r} g(r) + \frac{b^2}{2} \int_b^\infty \frac{dr}{r^3} g(r). \quad (\text{C3}) \end{aligned}$$

The benefit of such a transformation is that each of the partial integrals may be handled independently, employing suitable approximations for each case.

The integral in the first line of (C3) converges very rapidly for  $r \gg b \rightarrow 0$  due to the first factor of the integrand. Hence, its small- $b$  asymptotics may be derived by just Taylor expanding the screening function

$$g(r) = g(0) + rg'(0) + \frac{r^2}{2}g''(0), \quad (\text{C4})$$

viz.,

$$\begin{aligned} & \int_b^\infty dr \left( \frac{1}{\sqrt{r^2 - b^2}} - \frac{1}{r} - \frac{b^2}{2r^3} \right) g(r) \\ & \underset{b \rightarrow 0}{\simeq} \left( \ln 2 - \frac{1}{4} \right) g(0) + \frac{b}{2} g'(0) + \frac{b^2}{8} (1 + 2 \ln 2) g''(0). \quad (\text{C5}) \end{aligned}$$

The second integral in (C3) diverges at  $b \rightarrow 0$  logarithmically. It can be reduced to a convergent one by a single partial integration

$$\int_b^\infty \frac{dr}{r} g(r) = -g(b) \ln b - \int_b^\infty dr g'(r) \ln r. \quad (\text{C6})$$

Granted that the latter integral remains finite in the limit  $b \rightarrow 0$ , it can be exactly supplemented to an integral beginning at  $r = 0$ :

$$\begin{aligned} \int_b^\infty \frac{dr}{r} g(r) = & -g(b) \ln b + \int_0^b dr g'(r) \ln r \\ & - \int_0^\infty dr g'(r) \ln r. \quad (\text{C7}) \end{aligned}$$

The first two terms may be rearranged by partial integration, if we substitute  $g'(r) = \frac{d}{dr}[g(r) - g(0)]$ , so that the bracket vanishes at the origin, canceling the  $1/r$  singularity:

$$\begin{aligned} \int_b^\infty \frac{dr}{r} g(r) = & -g(0) \ln b \\ & - \int_0^b \frac{dr}{r} [g(r) - g(0)] - \int_0^\infty dr g'(r) \ln r. \quad (\text{C8}) \end{aligned}$$

Small- $b$  expansion of the latter structure is now readily obtained by inserting the Taylor expansion (C4) into the middle integral:

$$\begin{aligned} \int_b^\infty \frac{dr}{r} g(r) \underset{b \rightarrow 0}{\simeq} & -g(0) \ln b - bg'(0) - \frac{b^2}{4} g''(0) \\ & - \int_0^\infty dr g'(r) \ln r. \quad (\text{C9}) \end{aligned}$$

The third integral in (C3) diverges at  $b \rightarrow 0$  quadratically. By triple integration by parts, it is reduced to a convergent one:

$$\begin{aligned} \frac{b^2}{2} \int_b^\infty \frac{dr}{r^3} g(r) &= \frac{1}{4} [g(b) + bg'(b)] \\ &\quad - \frac{b^2}{4} g''(b) \ln b - \frac{b^2}{4} \int_b^\infty dr g'''(r) \ln r. \end{aligned} \quad (\text{C10})$$

Within the required accuracy, the lower limit of the last integral may merely be replaced by 0, while in the second term, it is justified to set  $g''(b) \simeq g''(0)$ . In the first term,  $g(b)$  needs to be Taylor expanded via Eq. (C4). Altogether, that gives

$$\begin{aligned} \frac{b^2}{2} \int_b^\infty \frac{dr}{r^3} g(r) &\underset{b \rightarrow 0}{\simeq} \frac{1}{4} \left[ g(0) + 2bg'(0) + \frac{3b^2}{2} g''(0) \right] \\ &\quad - \frac{b^2}{4} g''(0) \ln b - \frac{b^2}{4} \int_0^\infty dr g'''(r) \ln r. \end{aligned} \quad (\text{C11})$$

Combining the pieces (C5), (C9), and (C11) of Eq. (C3) and collecting the like terms, we get the subleading small- $b$  asymptotics of  $S_0(b)$ ,

$$S_0 \underset{b \rightarrow 0}{\simeq} \ln \frac{b}{b_0} + \frac{b^2}{4} \int_0^\infty dr g'''(r) \left( \ln \frac{2r}{b} + 1 \right), \quad (\text{C12})$$

where  $b_0$  is given by Eq. (46).

## 2. Classical scattering

Putting (C12) into (C1) and differentiating, we are led to the representation

$$Q(b) = \frac{\partial}{\partial b} S_0(b) = \frac{1}{b} + \frac{b}{2} \int_0^\infty dr g'''(r) \left( \ln \frac{2r}{b} + \frac{1}{2} \right) \quad (\text{C13})$$

for the subleading small- $b$  asymptotics of the indicatrix. It features a  $\ln b$  factor in the subleading term and upon inversion as

$$b^2(Q) = \frac{1}{Q^2} + \frac{1}{Q^4} \int_0^\infty dr g'''(r) \left( \ln 2Qr + \frac{1}{2} \right) \quad (\text{C14})$$

and substitution into (28) leads to a result

$$\frac{d\sigma}{d\sigma_R} = 1 + \frac{1}{Q^2} \int_0^\infty dr g'''(r) \left( 2 \ln 2Qr + \frac{1}{2} \right) \quad (\text{C15})$$

similar to Molière's (70), with

$$\mu_0^2 = g''(0). \quad (\text{C16})$$

However, if the condition (8) is valid, the term containing  $\ln Q$  vanishes [ $\int_0^\infty dr g'''(r) = -g''(0) = 0$ ], whereby we return to our Eqs. (72) and (76).

## 3. Quantum scattering

In the quantum calculation we expand

$$\begin{aligned} e^{2i\alpha S_0(b)} &\simeq \left( \frac{b}{b_0} \right)^{2i\alpha} \left[ 1 + \frac{i\alpha}{2} b^2 \int_0^\infty dr g'''(r) \left( \ln \frac{2r}{b} + 1 \right) \right] \\ &= \left( \frac{b}{b_0} \right)^{2i\alpha} + \frac{i\alpha}{2} \left[ \int_0^\infty dr g'''(r) \ln \frac{2r}{b_0} \right. \\ &\quad \left. - g''(0) \left( 1 + \frac{i}{2} \frac{\partial}{\partial \alpha} \right) \right] b^2 \left( \frac{b}{b_0} \right)^{2i\alpha}. \end{aligned} \quad (\text{C17})$$

Inserting this into the impact parameter representation (39) for the scattering amplitude, carrying out the integration by the formula (B8), and subsequently differentiating by  $\alpha$ , we obtain a structure similar to (70) again, but this time with  $\mu_1$  depending on  $\alpha$ .

- 
- [1] N. F. Mott and H. Massey, *The Theory of Atomic Collisions*, 3rd ed. (Oxford University Press, London, 1965).
- [2] L. D. Landau and E. M. Lifshitz, *Quantum Mechanics: Nonrelativistic Theory*, 2nd ed. (Pergamon, London, 1965).
- [3] E. Weigold and I. E. McCarthy, *Electron Momentum Spectroscopy* (Springer Science + Business Media, New York, 1999).
- [4] R. F. Egerton, *Electron Energy-Loss Spectroscopy in the Electron Microscope* (Springer, New York, 2011).
- [5] A. O. Hanson, L. H. Lanzl, E. M. Lyman, and M. B. Scott, *Phys. Rev.* **84**, 634 (1951).
- [6] H. Knudsen, F. Besenbacher, J. Heinemeier, and P. Hvelplund, *Phys. Rev. A* **13**, 2095 (1976).
- [7] H. H. Andersen, J. Bøttiger, and H. Knudsen, *Phys. Rev. A* **7**, 154 (1973).
- [8] H. Knudsen and P. Møller Petersen, *Radiat. Eff.* **28**, 147 (1976); *J. Phys. B* **11**, 455 (1978).
- [9] E. Huttel, W. Arnold, H. Baumgart, and G. Clausnitzer, *Nucl. Instrum. Methods Phys. Res. Sect. B* **12**, 193 (1985).
- [10] J.-P. Connerade, *Highly Excited Atoms* (Cambridge University Press, Cambridge, 1998).
- [11] J. Sapirstein, *Rev. Mod. Phys.* **70**, 55 (1998).
- [12] K. T. Moore and G. van der Laan, *Rev. Mod. Phys.* **81**, 235 (2009).
- [13] G. Rayner-Canham, *The Periodic Table: Past, Present, and Future* (World Scientific, Singapore, 2020).
- [14] E. Scerri, *The Periodic Table: Its Story and Its Significance*, 2nd ed. (Oxford University Press, Oxford, 2020).
- [15] V. B. Berestetskii, E. M. Lifshitz, and L. P. Pitaevskii, *Quantum Electrodynamics* (Pergamon, Oxford, 1982).
- [16] A. I. Akhiezer and V. B. Berestetskii, *Quantum Electrodynamics* (Nauka, Moscow, 1981).
- [17] T. Kato, *Commun. Pure Appl. Math.* **10**, 151 (1957).
- [18] W. A. Bingel, *Z. Naturforsch. A* **18**, 1249 (1963).
- [19] N. H. March, *Self-Consistent Fields in Atoms: Hartree and Thomas-Fermi Atoms* (Elsevier, Amsterdam, 2016).
- [20] I. Lobato and D. Van Dyck, *Acta Cryst. A* **70**, 636 (2014).
- [21] P. A. Doyle and P. S. Turner, *Acta Cryst. A* **24**, 390 (1968).

- [22] P. Sigmund, *Particle Penetration and Radiation Effects Vol. 2. Penetration of Atomic and Molecular Ions* (Springer, New York, 2014).
- [23] A. I. Akhiezer and N. F. Shul'ga, *High Energy Electrodynamics in Matter* (Gordon & Breach, Amsterdam, 1996).
- [24] J. D. Jackson, *Classical Electrodynamics*, 3rd ed. (Wiley, New York, 1999).
- [25] H. Fleischmann, *Z. Naturforsch. A* **15**, 1090 (1960).
- [26] W. T. Scott, *Rev. Mod. Phys.* **35**, 231 (1963).
- [27] J. Lindhard, V. Nielsen, and M. Scharff, *Mat.-Fys. Medd. Dan. Vid. Selsk.* **38**, 1 (1968).
- [28] G. Molière, *Z. Naturforsch. A* **2**, 133 (1947).
- [29] N. F. Mott and W. L. Bragg, *Proc. R. Soc. London Ser. A* **127**, 658 (1930).
- [30] H. Bethe, *Ann. Phys. (Leipzig)* **397**, 325 (1930).
- [31] L. C. Allen and E. T. Knight, *Int. J. Quantum Chem.* **90**, 80 (2002).
- [32] D. P. Wong, *J. Chem. Educ.* **56**, 714 (1979).
- [33] V. N. Ostrovsky, *J. Phys. B* **14**, 4425 (1981).
- [34] E. D. Belokolos, *SIGMA* **13**, 038 (2017).
- [35] A. Sommerfeld, *Atomic Structure and Spectral Lines*, 3rd ed. (Methuen, London, 1934).
- [36] M. Goeppert Mayer, *Phys. Rev.* **60**, 184 (1941).
- [37] B.-G. Englert and J. Schwinger, *Phys. Rev. A* **32**, 47 (1985).
- [38] U. Fano, C. E. Theodosiou, and J. L. Dehmer, *Rev. Mod. Phys.* **48**, 49 (1976).
- [39] E. B. Kolomeisky and M. Timmins, *Phys. Rev. A* **72**, 022721 (2005).
- [40] D. Ward, H. R. Andrews, L. V. Mitchell, W. N. Lennard, R. B. Walker, and N. Rud, *Can. J. Phys.* **57**, 645 (1979).
- [41] W. N. Lennard, H. Geissel, D. P. Jackson, and D. Phillips, *Nucl. Instrum. Methods Phys. Res. Sect. B* **13**, 127 (1986).
- [42] F. Besenbacher, J. Böttiger, T. Laursen, P. Loftager, and W. Möller, *Nucl. Instrum. Methods* **170**, 183 (1980).
- [43] H. Winter, C. Auth, A. Mertens, A. Kirste, and M. J. Steiner, *Europhys. Lett.* **41**, 437 (1998).
- [44] L. Eriksson, J. A. Davies, and P. Jespersgaard, *Phys. Rev.* **161**, 219 (1967).
- [45] F. H. Eisen, *Can. J. Phys.* **46**, 561 (1968).
- [46] M. K. Linnarsson, L. Vines, and A. Hallen, *J. Appl. Phys.* **130**, 075701 (2021).
- [47] W. Scandale and A. M. Taratin, *Phys. Rep.* **815**, 1 (2019).
- [48] A. V. Korol, A. V. Solov'yov, and W. Greiner, *Channelling and Radiation in Periodically Bent Crystals* (Springer, Heidelberg, 2014).
- [49] M. V. Bondarenco, *Phys. Rev. Accel. Beams* **23**, 031303 (2020).
- [50] M. V. Bondarenco, *Phys. Rev. ST Accel. Beams* **15**, 032802 (2012).
- [51] H. A. Bethe and E. E. Salpeter, *Quantum Mechanics of One- and Two-Electron Atoms* (Academic, New York, 1957).
- [52] I. K. Dmitrieva and G. I. Plindov, *Z. Phys. A* **305**, 103 (1982).
- [53] E. Clementi and C. Roetti, *At. Data Nucl. Data Tables* **14**, 177 (1974).
- [54] Y. Tal and M. Levy, *J. Chem. Phys.* **72**, 4009 (1980).
- [55] J. C. Angulo, J. S. Dehesa, and F. J. Galvez, *Phys. Rev. A* **42**, 641 (1990).
- [56] J. P. Desclaux, *At. Data Nucl. Data Tables* **12**, 311 (1973).
- [57] S. K. Suslov, *J. Phys. B* **42**, 185003 (2009).
- [58] V. M. Burke and I. P. Grant, *Proc. Phys. Soc.* **90**, 297 (1967).
- [59] G. Molière, *Z. Naturforsch. A* **3**, 78 (1948).
- [60] H. A. Bethe, *Phys. Rev.* **89**, 1256 (1953).
- [61] L. N. Cooper and J. Rainwater, *Phys. Rev.* **97**, 492 (1955).
- [62] M. V. Bondarenco, *Eur. Phys. J. C* **82**, 870 (2022).
- [63] M. V. Bondarenco, *Phys. Rev. D* **93**, 036008 (2016); **94**, 119901(E) (2016).
- [64] E. Fermi, *Rend. Acad. Naz. Lincei* **6**, 602 (1927).
- [65] E. B. Baker, *Phys. Rev.* **36**, 630 (1930).